Magnetoelectric Effects in $MnBi_2Te_4$, an antiferromagnetic topological insulator

Eric Soriano Baguet

Bachelor's Degree in Engineering Physics
and
Bachelor's Degree in Mathematics

Advisor

Prof. Pablo Jarillo-Herrero

Co-Advisor

Prof. Cristobal Voz Sanchez

May 2020

Abstract

In this project, we focus on the fabrication of Van der Waals heterostructures of $MnBi_2Te_4$ with different thicknesses, an antiferromagnetic topological insulator, using mechanical exfoliation and pick up transfer methods. We will create devices using Ebeam lithography, among other techniques, and using a Hall-bar-shaped device we will analyze the different magnetic properties we can observe controlling the electric field. These effects are known as magnetoelectric effects. We study electronic transport properties at low temperature and under a magnetic field. Second Harmonic Generation and Nitrogen-Vacancy center collaborations are also realized in order to see the magnetization of the material.

AMS codes: 81-01, 82-02

Keywords: Condensed matter, Solid-state physics, Topological insulator, Antiferromagnetism, Magnetoelectric effects, Van der Waals heterostructures, Nanofabrication, Two dimensional materials, $MnBi_2Te_4$, graphene, Anomalous Hall Effect, Electric Field model, SHG, N-V center.

Acknowledgements

First of all, I am very grateful to Prof. Pablo Jarillo-Herrero for giving me the opportunity to join his group at MIT and to be working in such an high-level laboratory since the first day.
I would also like to thank all the research group for helping and accompanying me in this learning journey, scientifically and personally speaking, specially Kenji Yasuda, my mentor in the PJH's group who has guided me through the whole stay and from whom I have learned so much, and Daniel Rodan and Oriol Rubies, my office mates, with whom I have spent such a great time.
I want to thank the Interdisciplinary Higher Education Center (CFIS) for this opportunity and their financial support, together with the Fundació Privada Cellex, without which this stay would have been impossible.
Thanks to all the people that I have met and have accompanied me in this travel, Michele, Jonas and Marta among others and those who I have gotten to know better, Guillem, Albert, Joan and Eric.
Lastly, I would like to thank my family, Sylvie, Salvador, David and Laetitia for their support, not only in this year but though my entire life and my best friends, Erwan, Paul F, Javier, Paul L, Eduard and Paula for their friendship and all that I have received from them.

Contents

Chapter 1

Introduction

This first section gives a short overview of the theoretical background behind the study of $MnBi_2Te_4$ and explains the objectives for the transport measurements.

1.1 Theoretical concepts

1.1.1 Magnetic Topological Insulators

Before explaining different properties of Topological Insulators and Magnetic Topological Insulators, we briefly introduce Hall effect.
The ordinary Hall effect (HE) is the appearance of a transverse voltage difference when an electric current flows through a conductor. The clearest example of it is to place a conductor under a perpendicular magnetic field and inject an electric current though it, as represented in Figure 1.1. The magnetic field will bent the electron trajectory due to the Lorentz force to one side of the conductor where they will start to accumulate, creating a potential (V_H) in the direction transverse to the current and the magnetic field. This potential will at some point stabilize since the accumulated electrons will repel the other electrons, reaching a steady state. This set-up is particularly relevant when we will work with electronic transport measurements, which consist of injecting a current and measuring voltage drops. The presence of Hall effect without an external magnetic field is known as Anomalous Hall effect (AHE).

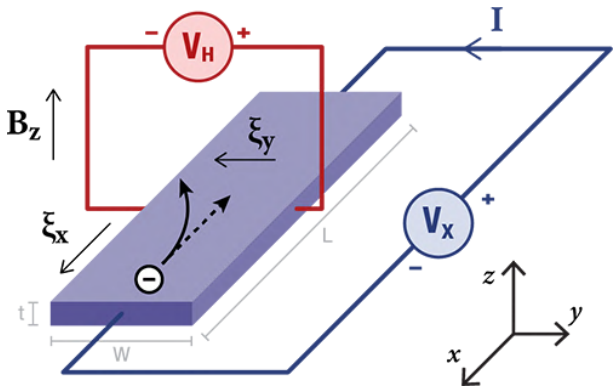

Figure 1.1: Example of ordinary Hall effect. Source: Lakeshore Crytronics

Topological Insulators (TI) are materials that act as insulators but can conduct electricity through their surface states. This is due to the gapless surface states laying in a bandgap on the bulk band structure (see Figure 1.2) [1]. Those states are symmetry-protected by time-reversal symmetry. Thus, the main property to take into account is that if the Fermi level is placed inside the bandgap of the bulk, the bulk is insulating but the surface of the material still allows the flow of a dissipation-less current (Figure 1.3b).
TI are being studied thanks to the topological band theory, an enhanced band theory which takes into account concepts such as Chern numbers and Berry phases. The term topological implies the existence of a bulk invariant (usually sets of numbers, such as the Chern numbers) that differentiates between phases of matter having the same symmetry. They are classified according to the rule that two states belong to the same class if one can be gradually converted into the other without gap closure and thus have the same set of numbers. [2]

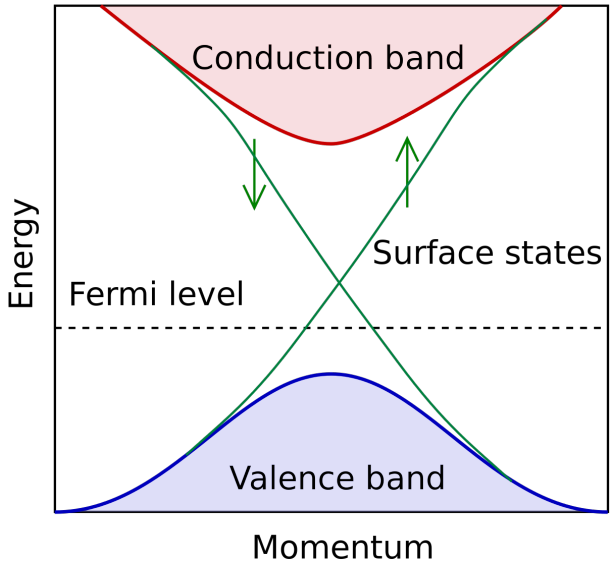

Figure 1.2: Schematics of the band structure of a Topological Insulator centered in the bandgap. Source: [3]

Another very interesting property of TI is that those surface states are topologically protected, therefore any continuous deformation of the surface would not alter the current flowing through it.

If a TI is placed inside a magnetic field, the time-reversal symmetry is broken and Landau levels are generated inside the bulk of the material and thus remains a insulator, but a current starts flowing at the edge of the material. This current in quantized, generating the so-called Quantum Hall Effect (QHE), being the quanta $\sigma = C\frac{e^2}{h}$, with e the electron charge, h the Planck constant and C the Chern number, a topological invariant of the material corresponding to the occupancy of the Landau levels [4]. This current has no dissipation and provokes the appearance of a Hall voltage. When a magnetic element is introduced inside a TI we obtain a Magnetical Topological Insulator (MTI). This insertion breaks the time-reversal symmetry and can create a chiral edge state flowing along the edge of the sample (see Figure 1.3d).

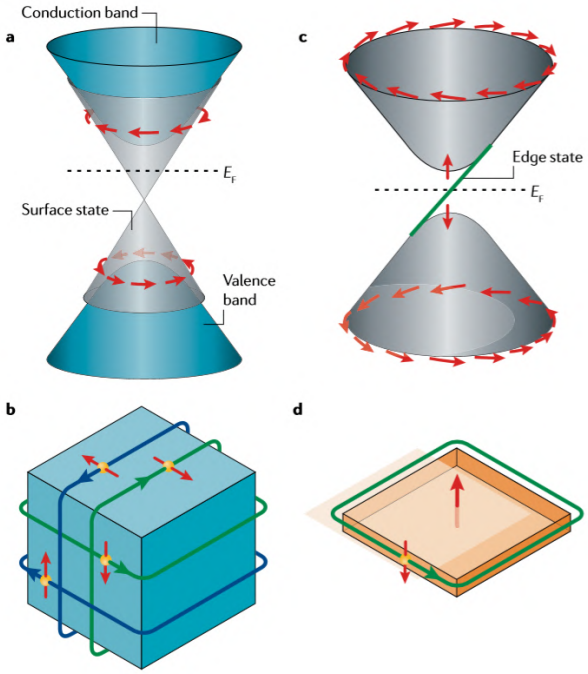

Figure 1.3: a) anb b) are Topological Insulators. a) The bulk valence and conduction bands and the massless Dirac-like dispersion of the surface state. b) Real-space picture of the surface states. Electron spins dictate the direction of the current.
c) and d) are Magnetic Topological Insulators. c) The gapped Dirac-like dispersion of the surface state. d) The chiral edge mode in MTI. Schematic taken from [4].

Since the MTIs have this chiral edge state at zero magnetic field due to their own internal magnetization, they can generate what is known as Quantum Anomalous Hall effect (QAHE), the quantized version of the AHE.

Figure 1.4 shows the first measurement of QAHE in $Cr_x(Bi_{1-y}Sb_y)_{2-x}Te_3$. Figure 1.4b presents a non-zero Hall resistivity at zero magnetic field, that changes sign depending on the direction of the sweeping of the magnetic field. Its quantization is controlled by a gate voltage V_g [4].

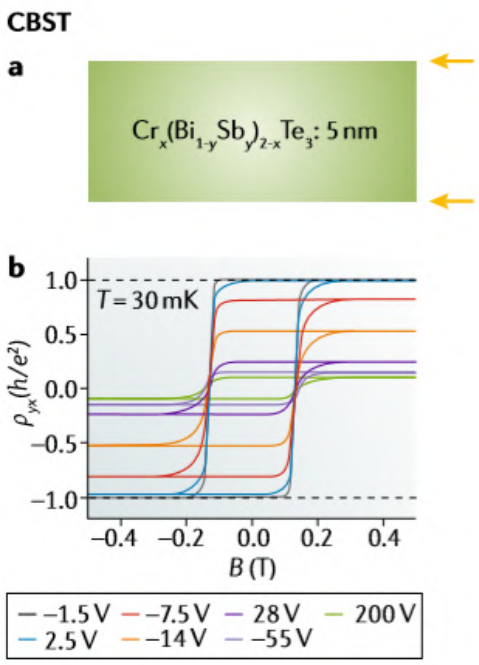

Figure 1.4: First example of Quantum Anomalous Hall Effect, measured in 5nm thick film of $Cr_x(Bi_{1-y}Sb_y)_{2-x}Te_3$. In b) measurements of the Hall resistivity ($\rho = 1/\sigma$). Source: [5].

1.1.2 $MnBi_2Te_4$, an antiferromagnetic topological insulator

Ferromagnetic (FM) Topological Insulators (i.e MTI with all magnetic moments pointing in the same direction), such as the one presented in Figure 1.4, have been investigated in the past decade. Recently, another type of MTI, $MnBi_2Te_4$ (MBT), has been found and is making a big impact in the condensed matter field due to the fact that it is an antiferromagnetic (AFM) Topological Insulator and can be exfoliated to 2D. AFM TI were previously "artificially" made by taking a TI and doping one layer with V and the other with Cr; this magnetization appears naturally in MBT, simplifying the fabrication part and opening a wide range of possibilities.

Bi_2Te_3 is a well-known TI and introducing an additional Mn-Te layer makes this material into a MTI, thanks to its own intrinsic magnetization. MBT has a tetradymite-type structure with the $R\bar{3}m$ space group and lattice constants a = 4.33 Å, c = 40.91 Å. It is organized in septuple layers (SL) of Te-Bi-Te-Mn-Te-Bi-Te (see Figure 1.5) with a total thickness of 14 Å. Each Mn^{2+} in high-spin configuration ($s = 5/2$) brings 5 μ_B magnetic moment, out of plane polarization. On a same Mn layer, all the spins are aligned FM, but the coupling between SL is AFM. The Néel temperature (T_N) is 24K in the bulk, 23K in 5SL and 18K in 3SL,

requiring the measurements to be performed at low temperatures. [6] [7] [8]

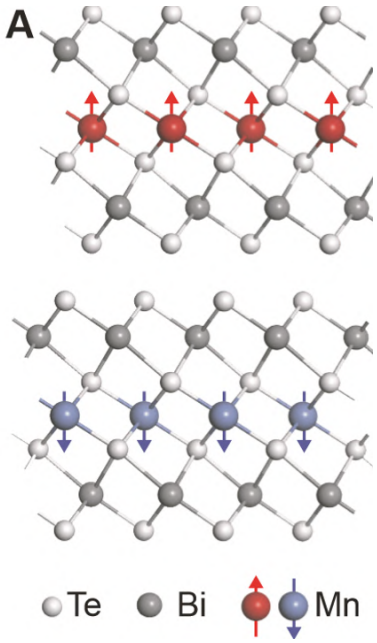

Figure 1.5: MBT structure. Here are depicted 2 SL. Source: [9].

The fact that this MTI is AFM permits different magnetic configurations: for example, in an even layered MBT at zero magnetic field (AFM configuration) we have zero net magnetization, since in each couple of SL, a layer "cancels" the others' magnetization. This state is called axion insulator: not allowing the current to flow along the edges. On the other side, if the sample is forced to be in a FM state (with a high magnetic field for example), there will be a net magnetization and therefore QAHE, obtaining a QAH insulator (the bulk is still insulating). Both states are depicted in Figure 1.6.
In the case of an odd layered sample, QAHE is measurable even without a magnetic field since there always is a net magnetization.
As presented in Figure 1.7, the switching of each layer can be observed when the sample is exposed to a high magnetic field, making possible the transition from the axion insulator state to the QAH insulator for even layered samples.

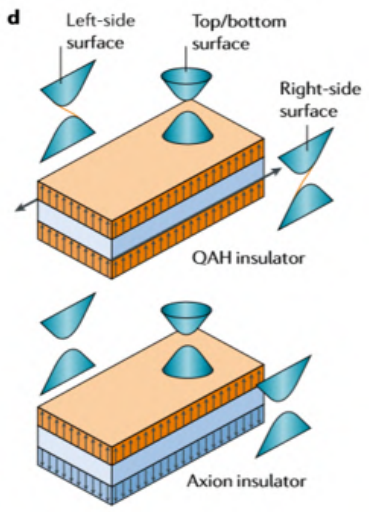

Figure 1.6: Two possible configurations for a bilayer AFM TI. These configurations can be reproduced in any sample with an even number of layers. Source: [4].

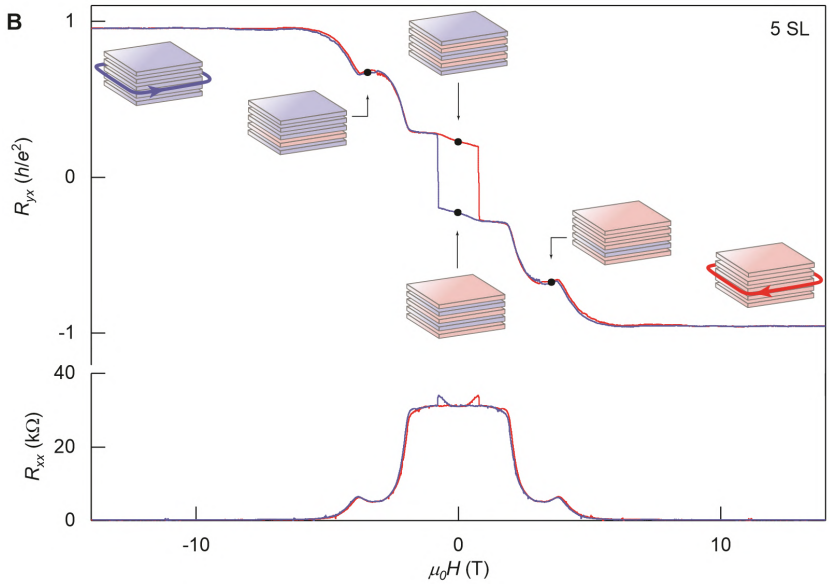

Figure 1.7: Switching of each layer in a 5SL layer thick sample thanks to a magnetic field. At the top is presented the Hall resistance (R_{yx}) and at the bottom the longitudinal resistance (R_{xx}) when sweeping a perpendicular magnetic field from left to right (red) and right to left (blue) at $T = 1.6$ K. When looking at the Hall resistance, the first thing that can be seen is the non-zero value at zero magnetic field, sign of the presence of QAHE (as expected from an odd layered sample). Then, the different plateaus can be observed coming from the switching of the magnetization of each layer (from FM due to a high magnetic field, to AFM, to FM again) and the sign of the Hall resistance at 0T is given by the sign of the FM magnetization of origin, creating this hysteresis loop, evidence of a net magnetization. Measurement from [9].

It is important to take into account that MBT seems to be sensitive to air, so we performed

all manipulations of the crystal and flakes inside a Ar-filled glovebox.

1.2 Objectives

This section presents the phenomena that we are planning to measure, not only during my stay at MIT but also in the long term.
The scope of the project is the effects of the electric field (E field) on the MBT and its magnetism, which are called topological magnetoelectric effects [4][10]. Three main effects will be addressed, inspired by previous measurements in other materials and by theoretical considerations on MBT.

1.2.1 Magnetization tuned by E field

The first objective is to tune the magnetization while maintaining the AFM state. This effect may be achieved by creating an unbalance between the layers thus provoking a non-zero net magnetization in the AFM state. The related effect has already been measured in bilayer CrI_3, it has been seen to be linear and that the sample appears to keep a certain "memory" from its previous FM state. See results in Figures 1.8 & 1.9 from papers [11] & [12] resp.

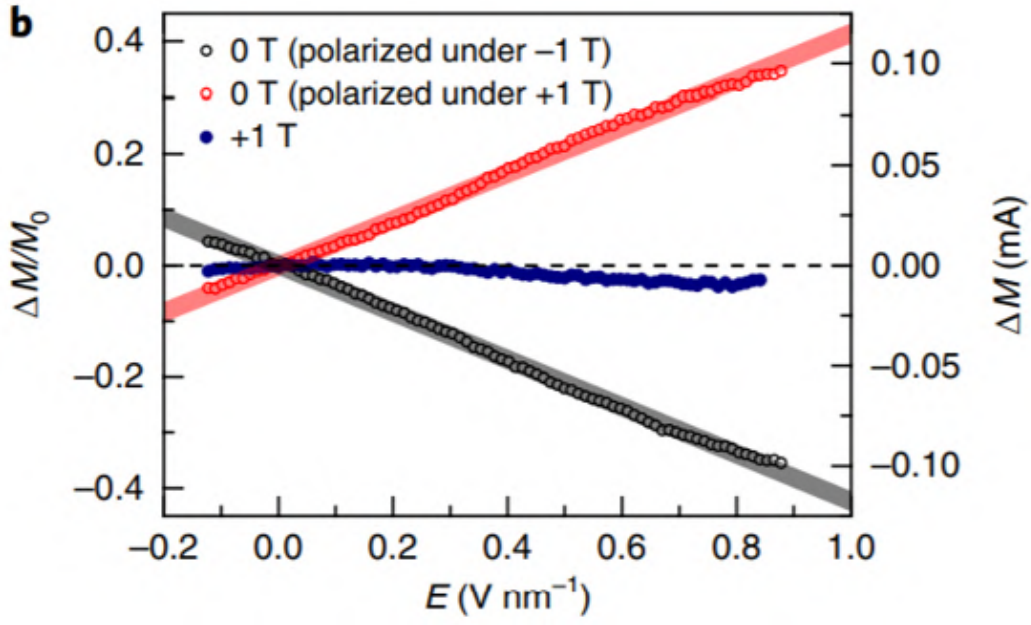

Figure 1.8: Magnetization induced by E field in bilayer CrI_3 in AFM state. Relative and absolute changes in the sheet magnetization ($\Delta M/M_0$ and ΔM, respectively) as a function of applied electric field measured under a fixed magnetic field. The broad lines are linear fits to the data at 0 T. Measurement from [11].

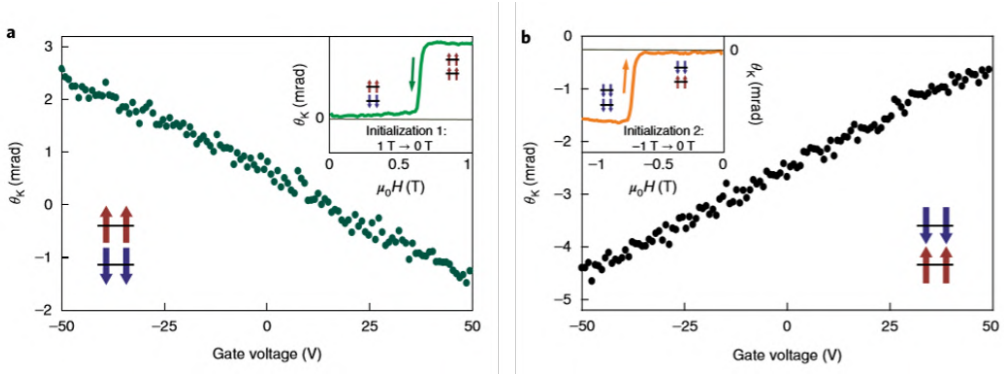

Figure 1.9: Magnetization induced by E field in bilayer CrI_3 in AFM state. Results obtained from Magneto-Optical Kerr Effect (MOKE) which is proportional to the magnetization of the sample. Insets show the initialization processes for preparing the antiferromagnetic states at zero magnetic field. Measurement from [12].

1.2.2 QAH/Axion insulator transition driven by *E* field

The second effect to be studied is the QAH/Axion insulator transition, but induced by E field. This result has already been measured using a magnetic field in [13] (measurements and comments in Figure 1.10) and the purpose is to check if it is possible to control this transition by E field, since E field is easier to apply that B field. The results obtained in bilayer CrI_3, a Van der Waals magnetic insulator (AFM in thin films), depicted in Figure 1.11, suggest that this could be achieved in MBT.

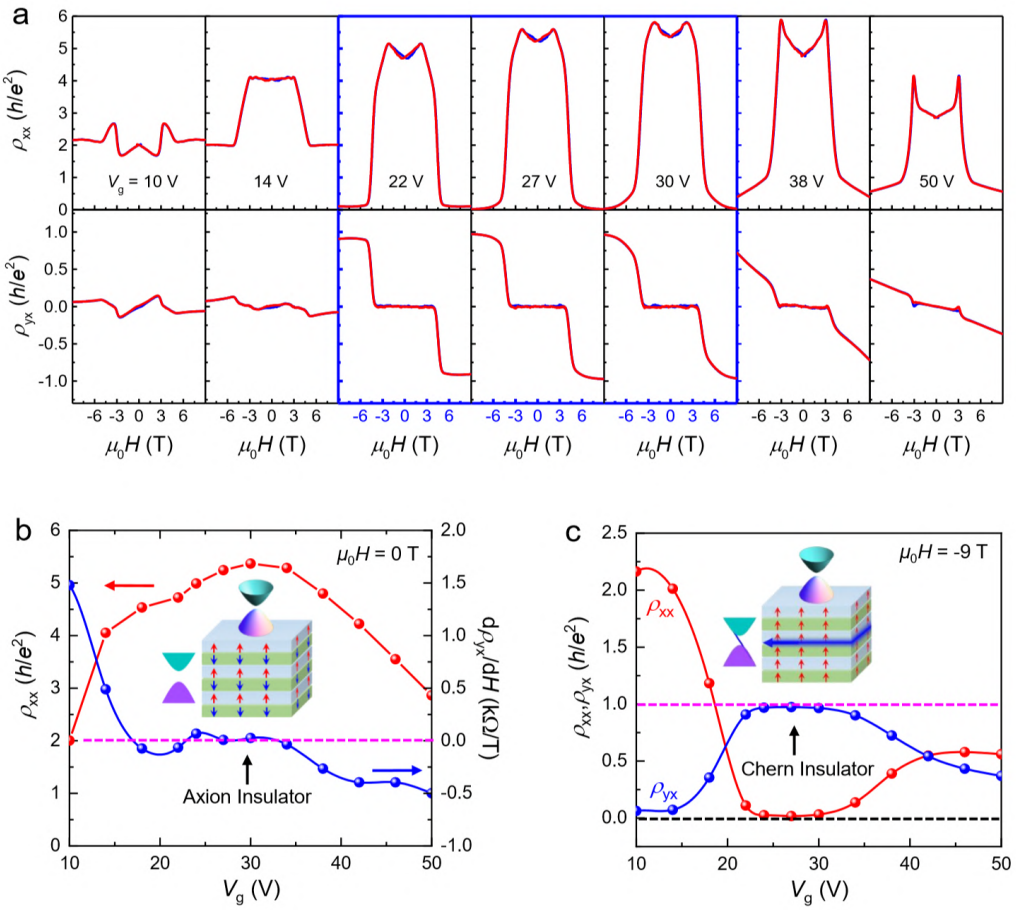

Figure 1.10: Measurements on a 6SL MBT at $T = 1.6$ K. a) Hall (ρ_{yx}) and longitudinal (ρ_{xx} resistivity while changing the gate voltage V_g. E_F is in the gap for $22V \leq V_g \leq 30V$, the blue box. The MBT thickness is confirmed to be even since the resistivity is 0 at zero B field. b) Reading the derivative of ρ_{yx} respect to the B field in blue, confirms that the sample is in the axion insulator state (i.e. there is no edge state). c) For a large magnetic field (so FM ordering), $\rho_{yx} = \frac{h}{e^2}$ when E_f is in the gap, the sample is in the Chern or QAH insulator state with a chiral edge state and $C = 1$. Measurement from [13].

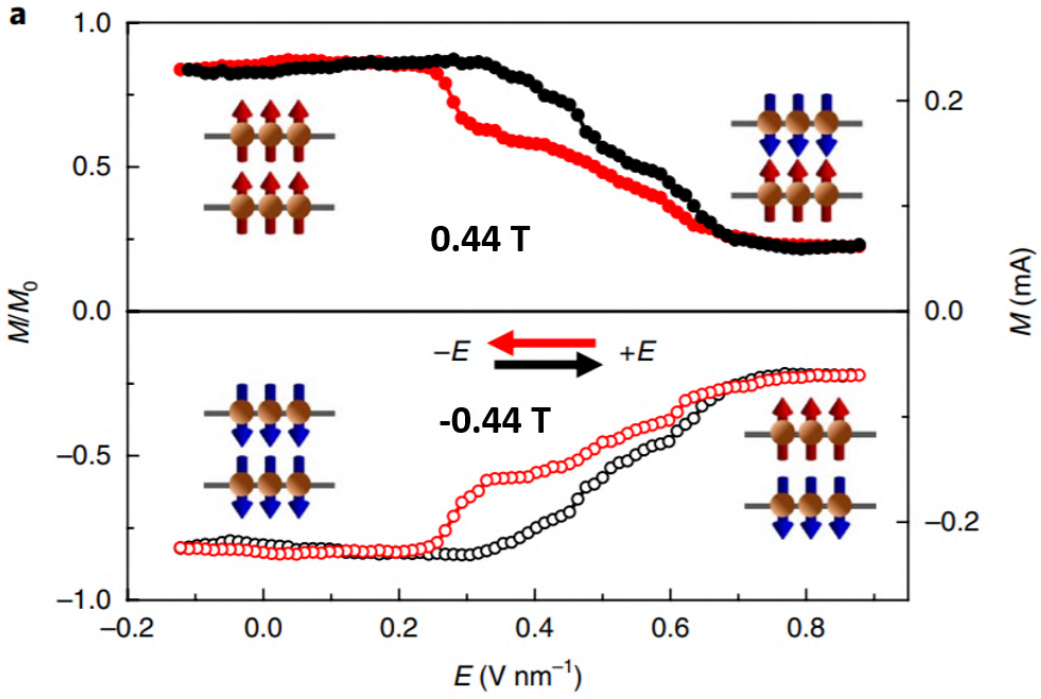

Figure 1.11: AFM/FM transition induced by E field in bilayer CrI_3. The FM states are forced by a B field (positive on top, negative on the bottom) and the magnetization of the sample M/M_0 is switched from FM to AFM and vice versa thanks to the E field. Measurement from [11].

1.2.3 QAH induced by E field in AFM state

This third and last goal is a very ambitious one. It is based on theoretical results on bilayer MBT that seem to indicate that the E field alters the band structure of MBT itself and could lead to a QAH insulator in zero B field, having a huge Hall resistance with a Chern number of 3. These theoretical results are presented in Figure 1.12.

An important theoretical detail is that, as we mentioned, the Chern number is a topological invariant, therefore should not change by continuous transformation of the band structure, but when the band gap closes and opens, there is a discontinuity and therefore the Chern number can vary. As we can see in Figure 1.12b, an area with a Chern number 3 could be attained (although experimentally difficult) at zero magnetic field.

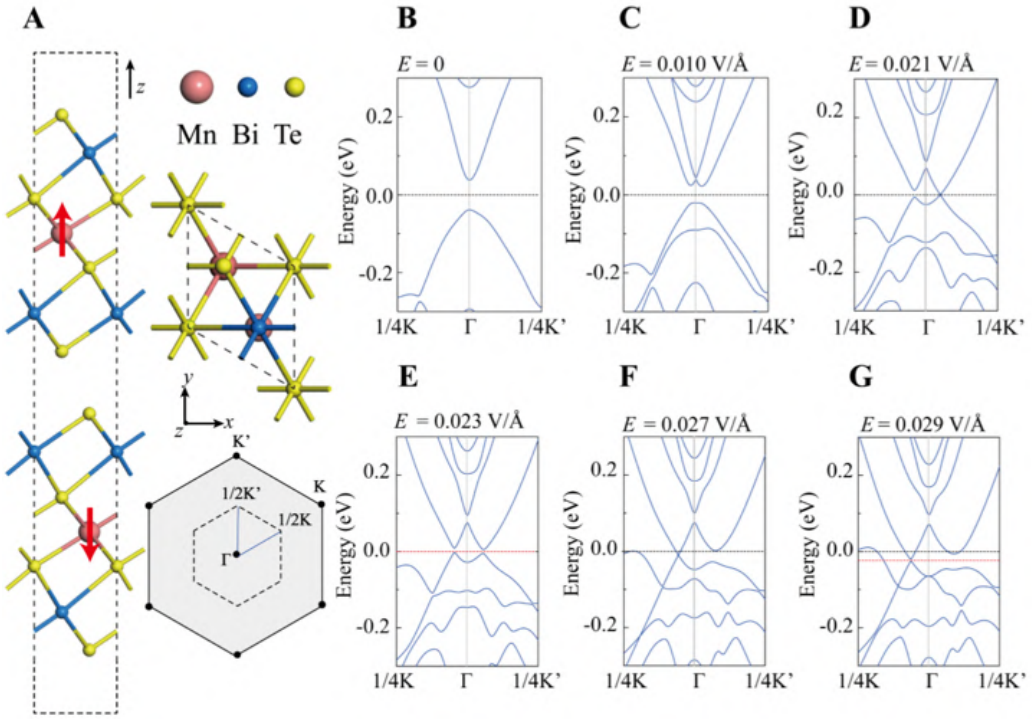

(a) A)The lattice structure of double-SL MnBi2Te4 thin film and the first BZ. B)-G) Band structures of double-SL $MnBi_2Te_4$ thin film under different electric fields. E_F is set to be zero. The closing and opening of the band gaps allow the Chern number, a topological invariant, to change.

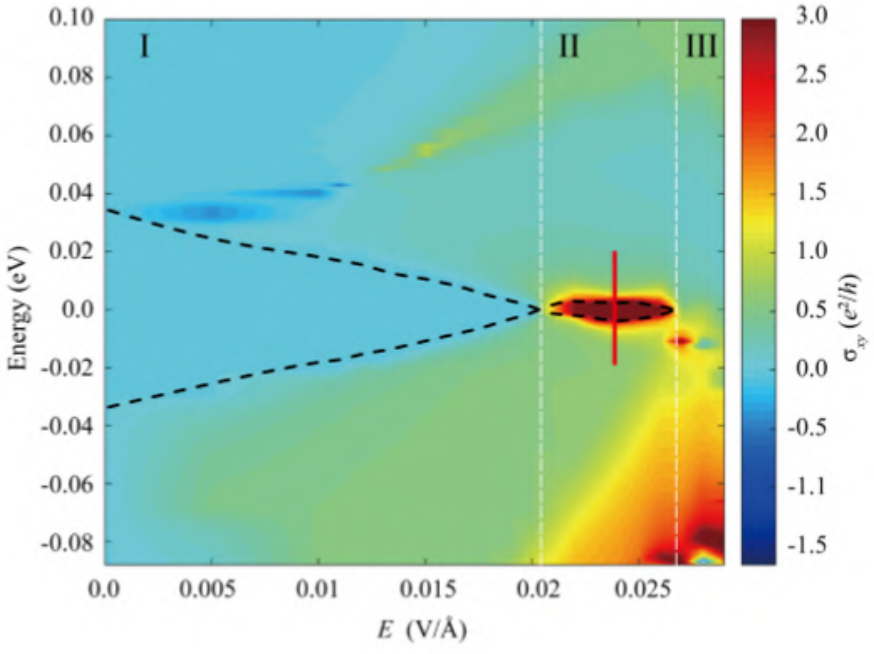

(b) Hall conductivity as a function of the E field and the energy. We can see three areas, having a $C = 3$ in area II at zero B field.

Figure 1.12: Theoretical results for bilayer MBT from [14] that conclude that we can obtain a Chern number of 3 at zero B field.

Once these phenomena are measured and can be reproduced, one of their many applications would be the creation of a memory device. For example, this material can transition from an axion insulator to a Chern insulator with Chern number up to 3. The state in which the sample is can be determined simply by measuring the Hall resistance, its presence being the state "ON" of the memory and its absence the "OFF" state (without electric field) [14]. This device would be useful since it would be a novel in the field but it also would allow to create low-consumption memory based in spintronics that could be used in Quantum Computing, for example.

Since our three objectives are related to E field, we modeled the E field inside an encapsulated MBT sample. The model and its results are included in Appendix A. An important conclusion from this modelling is that, for having a large range of values for E, we need thin MBT samples, from 2 to 4SL.

Chapter 2

Nanofabrication

This chapter explains the different processes of nanofabrication that we used to fabricate the MBT devices. They will first be presented in a non-chronological order, following the steps that were implemented to improve the devices. The section 2.6 will sketch a short summary of the whole nanofabrication procedure in chronological order. Note that MBT is air-sensitive so we conducted all the manipulations of MBT inside the glovebox, which made the fabrication more complex.

2.1 Exfoliation of the crystal

Exfoliation is the method used to obtain 2D flakes from the original bulk crystal. A metaphor often used to illustrate 2D materials is the following: the bulk crystal is similar to a very large dictionary (a 3D structure) and the exfoliation process allows to cleave some pages out of the dictionary, obtaining individual o thin stacks of pages that are called flakes (the 2D material).
For the fabrication of the devices we used three different 2D materials: hBN, graphite and finally MBT.
For hBN and graphite, the exfoliation method is called mechanical exfoliation and is straightforward: the crystal is placed on a tape (with variable stickiness depending on the selected material) and, pressing repetitively the material between two tapes, we cleave it until getting a uniform and dense pattern we deposit that on top of a Si/SiO_2 substrate, the main substrate we use in our MIT lab. This substrate or chip is made of Si with a 285nm thick SiO_2 layer on top, giving it a purple color. The process of exfoliation has variable parameters such as temperature, strength of the deposition or speed of the the tape's peeling (that can be controlled by a "peeling machine").
The exfoliation method for MBT is recent and more complex. Since this material had never been treated in our lab, we started trying the same methods as for graphite and hBN, varying

the above-mentioned parameters. The results were not dense enough and the flakes too thick. We then tried to evaporate a thin layer of Ti/Al_2O_3 on top of the substrate (first 0.2nm of Ti and then 7nm of Al_2O_3, also called AlOx) thanks to an e-beam evaporator to make it stickier (more details on evaporation will be made in section 2.4). The results were slightly better but still not dense enough and the exfoliated flakes were too thick. We used this method for the first devices but we rapidly moved onto another technique.
The next exfoliation technique, the Al_2O_3 assisted technique, was first described in the paper [15] for $Fe_{3x}GeTe_2$ and later was used on MBT with successful results [9]. The method is detailed here below and graphically described in Figure 2.1.

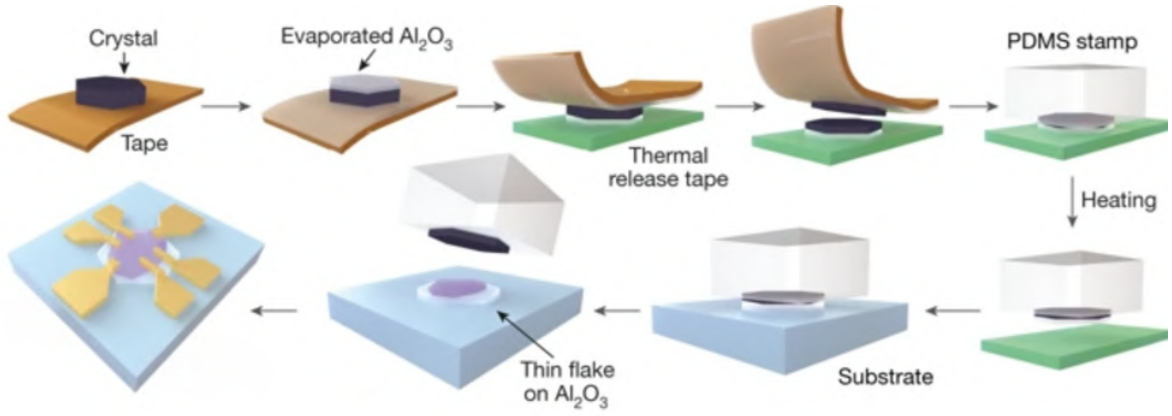

Figure 2.1: Al_2O_3 assisted exfoliation technique [15]

The Al_2O_3 assisted exfoliation technique works as following: we exfoliate the crystal on a kapton tape (that resist high temperatures) and introduced it in an e-beam evaporator; we slowly evaporate 50nm of Al_2O_3 on top on the tape and flakes; later on we exfoliate this stack on a thermal-release tape, cleaving the material (thus getting thinner flakes); then in order to move the stack of Al_2O_3/MBT to the Si substrate, we use as intermediary a Polydimethylsiloxane (PDMS) stamp to flip the stack and put the MBT on top. PDMS turns out to be very useful for flakehunting since the contrast is much higher on PDMS than on the Si substrate, as shown in Figure 2.2. Finally we deposit our PDMS stamp on the Si substrate and transfer the flake, since Van der Waals' interaction is stronger with the substrate than with PDMS. Note that there is still 50nm of Al_2O_3 under the MBT flakes.

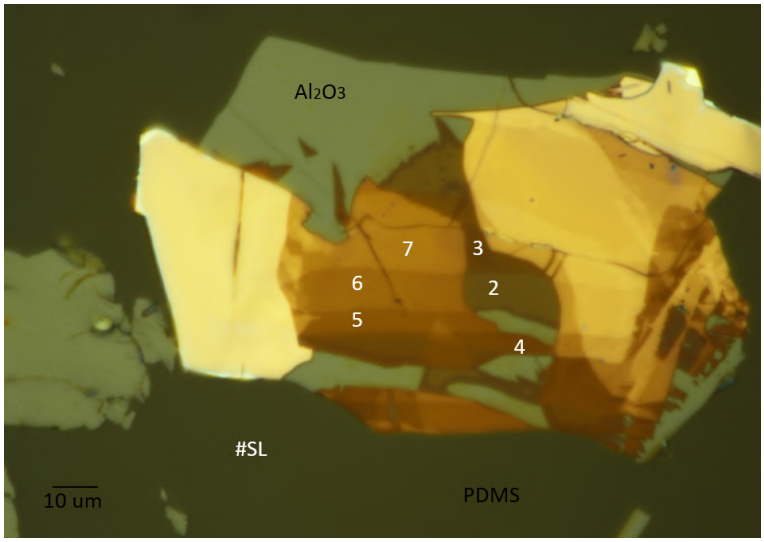

(a) MBT flake on PDMS

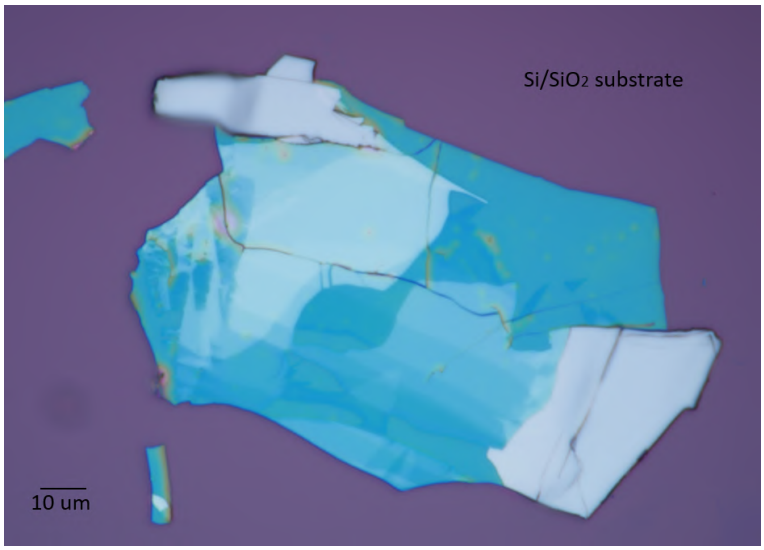

(b) MBT flake on Si/SiO_2 subtrate

Figure 2.2: Comparison for a flake obtained by the Al_2O_3 assisted exfoliation technique between the PDMS (a) and the Si/SiO_2 (b) substrate. The flake is flipped (as expected, see Figure 2.1). The contrast is much lower on the Si substrate, due to the fact that the color is mostly given by light interference on the Si/SiO_2 interface and thus the thickness of the flake: the Al_2O_3 layer is already 50nm thick and each additional MBT layer only contributes 1.4nm to that thickness. Meanwhile on PDMS we see the actual color of the flake. Also note that on the PDMS, the MBT is actually underneath the Al_2O_3, which is helpfully transparent.

When we compare the results of this technique to the previous one, the difference is astonishing (Figure 2.3): not only the obtained flakes are thinner, but they also are larger and more homogeneous.

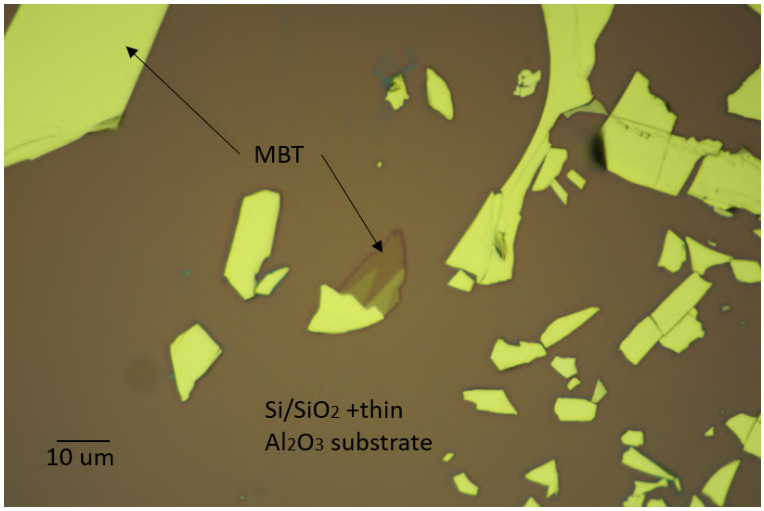

(a) Flake obtained using old exfoliation technique

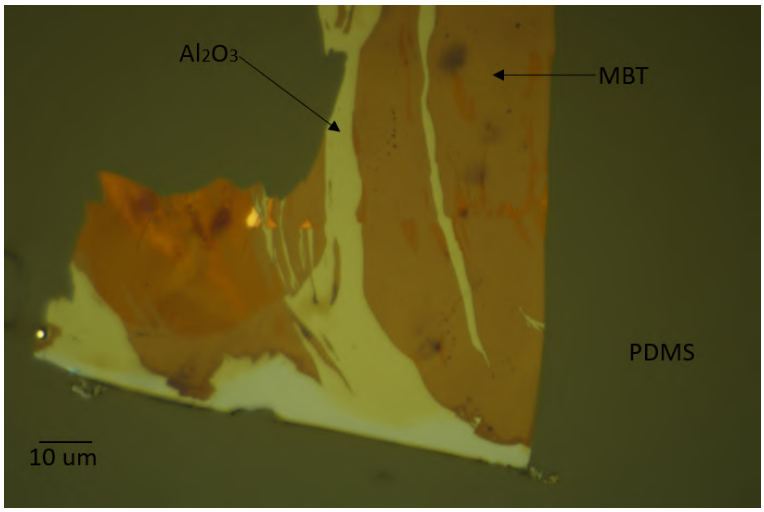

(b) Flake obtained using the Al_2O_3 assisted exfoliation technique

Figure 2.3: Comparison of flakes between original (a) and Al_2O_3 assisted (b) exfoliation technique. On the first picture, the flake is smaller and is actually 10nm thick, so $\tilde{7}$SL, while on the second one, the flake in around 3nm thick (2SL) on the indicated part. As the number of layers changes, so does the contrast. The white-ish shape on the bottom picture is the naked Al_2O_3 and the brownish part is MBT, with different thickness depending on the color (here from 2 to 5 SL). Picture (b) is shows the flake on PDMS and not on Si substrate for easier contrast.

Once the material is exfoliated, the chips (or PDMS for the Al_2O_3 assisted method) need to be flakehunted, meaning searched through the microscope to find potentially usable flakes (in our case the microscope is in the glovebox and can be used remotely). Before this step, the prerequisites for the flakes need to be established, such as: size, thickness or shape. The thickness is determined by contrast on the PDMS after a first flake with a lot of different thicknesses has been studied thanks to an Atomic Force Microscope and then used as calibration (in case of doubt, the thickness can be checked using a conversion of the picture to

grey-scale). Before the Al_2O_3 assisted method, we directly used the AFM.

2.2 Stacking

Nowadays the study of 2D materials is closely related to the study of Van der Waals structures: piles of different materials, stacked as we would stack LEGO pieces (see schematic in Figure 2.4). Different materials are used, some as main material to be studied (MBT in our case) and others for the properties they bring to the structure. The most frequent ones are hBN and graphite or graphene. Two dimensional hexagonal boron nitride (hBN) is used for its insulating properties and for protecting the flake under study to be in contact with the media. For that reason it is common to insert the material between two larger flakes of hBN, as in a sandwich. Graphene or graphite can be used as conductors. A very typical practice is to put a long graphene or graphite flake on top of the previously mentioned sandwich, forming a top gate. By putting that flake at a certain potential through an electric contact, we can apply electric field to the material through hBN.

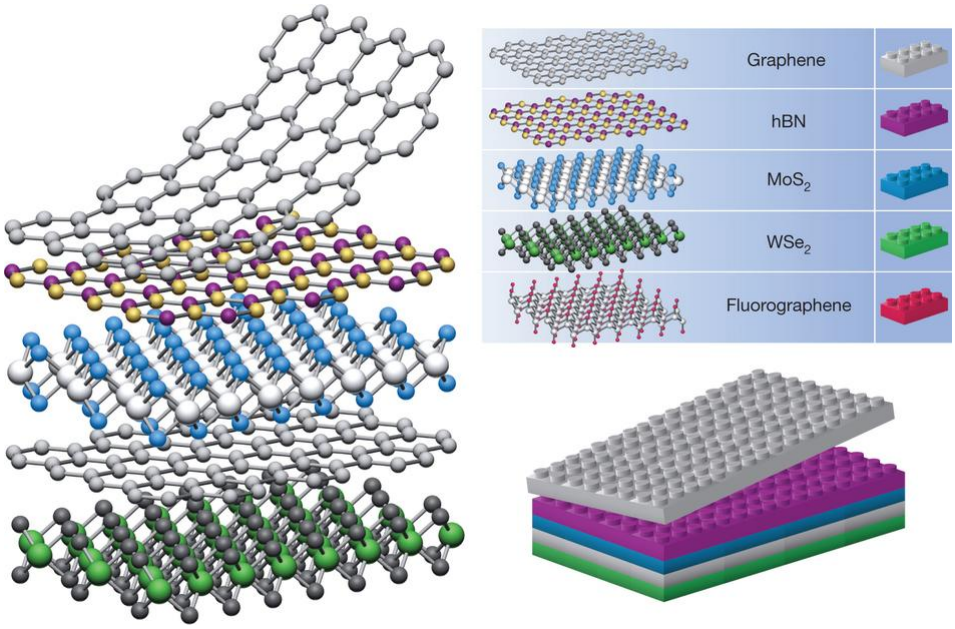

Figure 2.4: Schematic of a Van der Waals structure, compared to a LEGO structure, using as materials: hBN, graphite, MoS_2 and WSe_2

For stacking we first need to fabricate polycarbonate (PC) slides. Those are microscope glass slides with a small square of PDMS covered by a PC film (the PDMS is used to give a sticky and soft surface to the PC film). The interesting property of the PC film is that, when heated, it gets stickier until reaching 165^{o}C, where it melts. The procedure for stacking is the following: we put the PC slide on the mobile arm of a transfer set-up, we fix the chip

with the flake to transfered on the other arm and we slowly make them contact controlling the PC arm. We then heat the chip, that heats the PC, making it stickier and we transfer the flake to the PC slide by pulling up again the mobile arm.

For creating a stack we first design the stack on AutoCAD, selecting different flakes we flakehunted following different parameters such as thickness of the components, shape, etc.. We then successively pick up the chosen flakes in reverse order with Van der Waals force (i.e. from top to bottom) with the PC slide, making sure they are aligned as we have designed (the chip arm can be rotated to fix the angle). After the successive flakes are picked up and stacked on the PC slide, we deposit them by melting the PC on the destination chip. The PC film is then easily removed using chloroform.

2.3 Design of MBT devices

The devices we want to build are called Hall bars, presented in Section 2.3.1. The steps that we have developed internally for achieving these devices for MBT are described in 2.3.2

2.3.1 Hall Bar

Figure 2.5 shows the Hall bars that we want to fabricate (with optional top and/or bottom gates) and that are often used in transport measurements. They allow to measure the longitudinal resistance (measuring the difference of voltage between the left or the right contacts in Figure 2.5) and the Hall resistance (measuring the difference of voltage between the top or the bottom contacts in Figure 2.5) while a current is flowing from source to drain. This shape allows to minimize the interference of the longitudinal resistance in the Hall resistance, since the current only flows in a straight line.

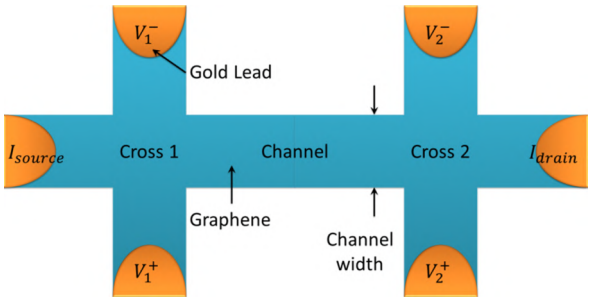

Figure 2.5: Scheme of a Hall Bar taken from [16]. We can see the drain and source, where the current is injected and then the 4 contracts for measurement, aligned. The contacts are usually made of gold or some combination of gold and another metal and they can easily be connected to the measurement set-up. A Hall bar with 5 contacts (missing one point of measurement) is also viable.

Additionally, we can add a top and/or a bottom gate to tune the electric field and/or the charge density in the material (we need both gates to tune independently both magnitudes since we need two degrees of freedom). Getting a device with a Hall bar shape can be achieved in two ways: the first (and ideal) one is to etch the flakes into that shape (we will see that in Section 2.5) and the second one is tip cleaning: we use a needle to scratch the material (in the transfer set-up for more precision) in order to shape it into a Hall bar. This method is very dangerous for the device, but faster.

2.3.2 Developed method

We use the nowadays well-known example of the twisted bilayer graphene as a example of device to highlight the intrinsic issues we face when creating our devices.

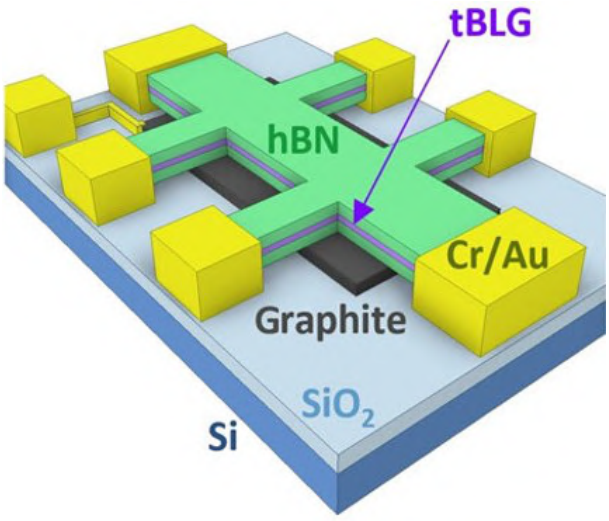

Figure 2.6: Stack of twisted bilayer graphene (tBLG) encapsulated between two hBN with a graphite back gate and Cr/Au contacts. Figure from [17]

The twisted bilayer graphene is put in a sandwich of hBN, for insulation and protection, with a metal or graphite back gate under the bottom hBN and an optional top gate (see Figure 2.6, although that device has no top gate). The shape of the material is a Hall Bar and the contacts are side contacts, meaning that the original stack has been etched, exposing the twisted graphene layer between the two hBN. Afterwards, metal is deposited on top, contacting the graphene by the recently exposed edges of the Hall bar.
That very effective and clean design is something that we wanted to implement as we advanced in our experiments but there are a couple of problems. First, we cannot encapsulate our device by the bottom part with hBN since there is already the thick layer of Al_2O_3 beneath the MBT, so a back gate would be difficult to implement. Secondly, we cannot make side contacts since our material is air-sensitive and, when moving the sample from the etching

to the evaporation machine, the device is exposed to air. This exposition, as our preliminary measurements showed, oxidizes the uncovered thin MBT region, turning it into a insulator and thus making the contacts inoperative.

We solved both problems in the following way:
-We decided to use the doped Si of the substrate itself as back gate,c called global back gate, which solved the first issue.
-The solution to the second problem is not so straightforward. Our first results indicated that while thin MBT (below 5SL) becomes insulating as it is exposed to air, thicker MBT does not. So we decided to look for flakes with thin layers for building our devices (2 to 4SL) but that were connected to regions with a thicker part (more than 5 SL). What we did is encapsulate the thin part with hBN and move the contacts to the thicker region of the sample. We also put a graphene flake on top of the hBN to use as a top gate (making sure that it is not in direct contact with the MBT). A schematic with the different steps is presented in Figure 2.7.
Unfortunately, due to the worldwide pandemic of Covid-19 and closing of the MIT, we only could apply this method to the last batch of devices.

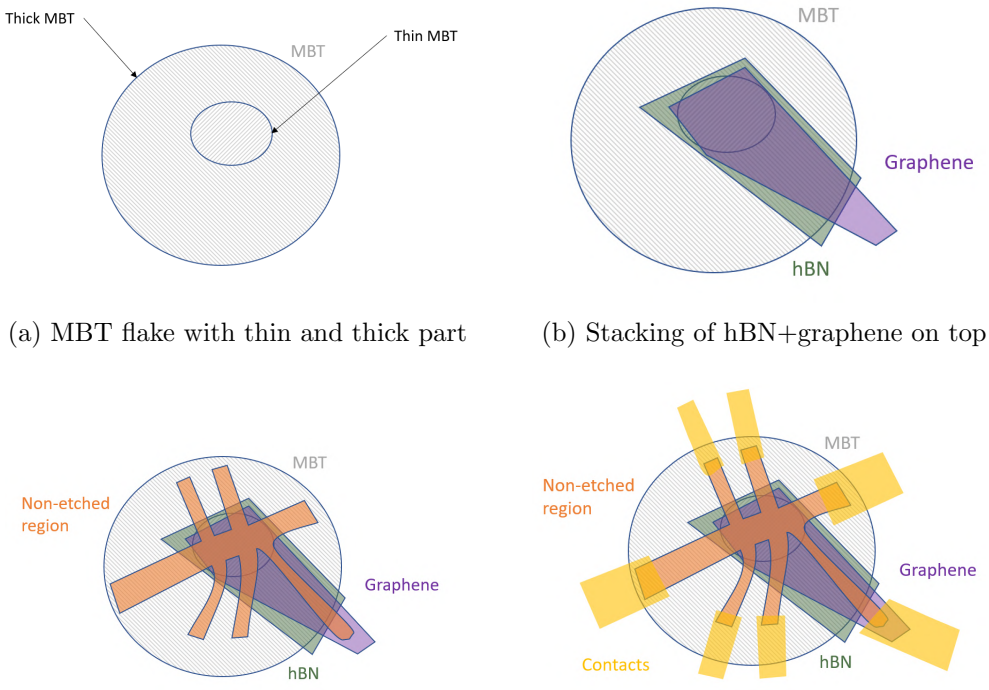

(a) MBT flake with thin and thick part

(b) Stacking of hBN+graphene on top

(c) Etching in Hall bar shape + top gate

(d) Evaporating the contacts

Figure 2.7: Developed fabrication process

The c) and d) steps of Figure 2.7 are detailed in Sections 2.4 & 2.5.

2.4 Evaporation of contacts

The contacts are metallic lines that allow to inject the current in the sample and measure the voltages at different points. They can be constituted by different metals (Au, Pt, Cr/Au, ...) and they go from the small contacts on the flake (down to 300 nm wide) to large pads (usually squares of 0.3x0.3 mm^2) that are connected to the chip holder thanks to wire bonding.
Metal can also be evaporated to create metallic back gates, evaporating a certain shape of metal and then depositing the stack on top of it, or top gates, evaporating the metal on top of the stack.

The process for obtaining metallic contacts on top of a stack is described in Figure 2.8 and is detailed further below. The fabrication of top or back gates uses the same method.

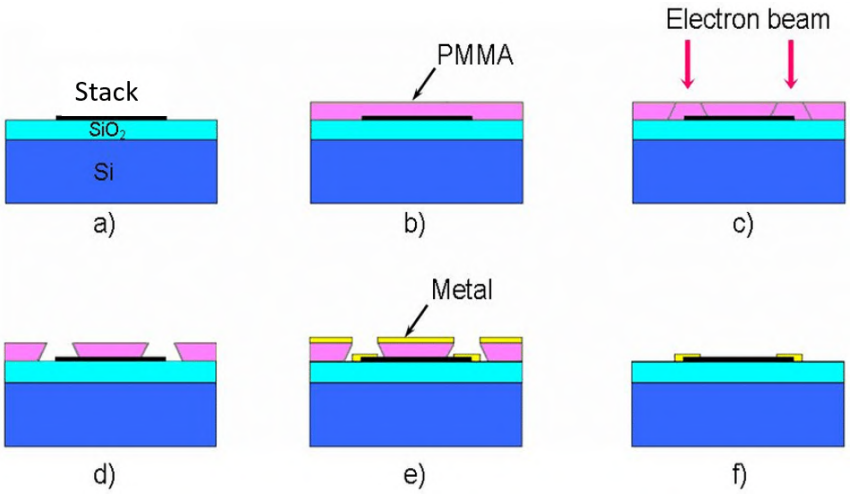

Figure 2.8: Steps for obtaining metallic contacts on top of a stack. The step d) is called development, the step e) evaporation and the step f) lift-off.

The steps in Figure 2.8 are the following:
-From a) to b) the substrate and whatever is on top is covered with PMMA -Poly(methyl methacrylate)- in one or two homogeneous layers.
-In c) the substrate covered in PMMA is exposed to an electron beam. At MIT we use Elionix, an Electron Beam Lithography System (EBL System), that allows us to expose a substrate following a pattern (designed in AutoCAD in our case). The substrate is aligned using markers that were previously deposited on it.
-In d), after exposure, PMMA is developped by putting the sample in cold water+IPA (Iso-Propyl Alcohol), removing the PMMA damaged by the e-beam.

-In e) the sample is placed in a thermal evaporator and the metal is deposited. The metal is deposited on top of the PMMA, except in the regions where is has been removed, where the metal touches directly the substrate or what is on top. For the MBT devices, we first evaporated Ti/Au for the contacts (0.5nm of Ti and then a few nm of Au), but after testing we moved to Cr/Au (0.5nm of Cr and then Au).
-Finally, in f), the PMMA is removed putting our sample in acetone for a few hours (lift-off). The PMMA is eliminated with the metal that was deposited on top of it, leaving the designed pattern by EBL in metal. The shape of the PMMA wells in d) and e) is important for avoiding "flags" of metal that could modify the pattern: if the walls were straight, some metal could lay on the walls of the well and when the PMMA would be removed, those pieces of metal could fall again on our sample, causing a change in the pattern or even contacts to touch each other.

Thanks to his fabrication method, 4 different types of contacts can be obtained:
-Top contacts: the contacts are evaporated on top on the stack, as in Figure 2.8.
-Edge contacts: if there is sandwich of hBN and our material inside, hBN can be etched, exposing the material in the center. When evaporating the contacts, the metal will contact it by the exposed areas on the sides. An example was given in Figure 2.6.
-Bottom contacts: it is possible to evaporate contacts with a Hall bar shape on top of an hBN and then deposit the stack on top of it. The metal is underneath the material but still contacts with it. This has the advantage that the material can be kept inside the glovebox until the device is finished.
-Via contacts: hBN can be etched to make holes in it and metal is deposited on those holes. This flake (and the gold covering the holes) can be stacked on top of the studied material to cover it. The contacts can be made from those metal points that touch the material through the hBN. This method is very long and costly, but can be useful for some materials. This method is depicted in Figure 2.9

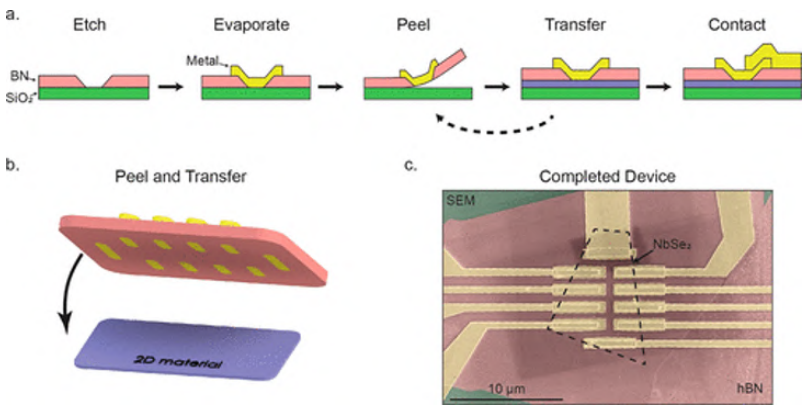

Figure 2.9: Schematic of the steps of via contacts and a picture of a device using this method. Figure from [18]

For the whole nanofabrication process we use two types of evaporator, thermal and e-beam evaporators. The thermal evaporator is used for depositing metals and the e-beam evaporator is used to deposit Al_2O_3 as part of the exfoliation method. Both methods are schematically described in Figure 2.10.

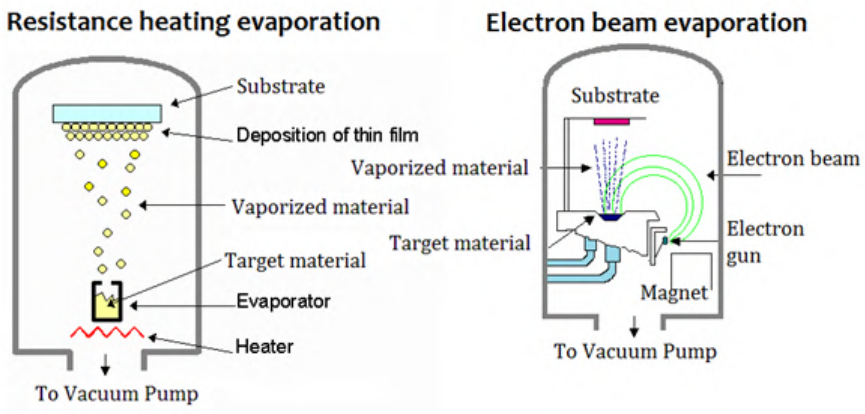

Figure 2.10: Comparison between e-beam and thermal (or resistance heating) evaporators. The substrate is sometimes submitted to rotation for a more uniform distribution of the deposited material

2.5 Etching

As mentioned, etching the device for giving it a Hall bar shape can improve the measurements, so we considered etching our MBT devices. This step has been introduced later on since a range of etching methods needed to be tested on MBT and it turned out to be a material difficult to etch.
The usual etching technique used in nanofabrication is Reactive Ion Etching (RIE, schematic using Fused Silica in Figure 2.11), a dry etching method. This method uses a plasma at low pressure (vacuum) that is generated by an electromagnetic field and the ions react with the substrate or a specific material, etching it away. Therefore a different recipe is needed for each material in order to have a successful reaction (in our case, graphite and hBN). Our preliminary results showed that MBT was not etched by RIE using old recipes and a "MBT-specific" recipe is in process.

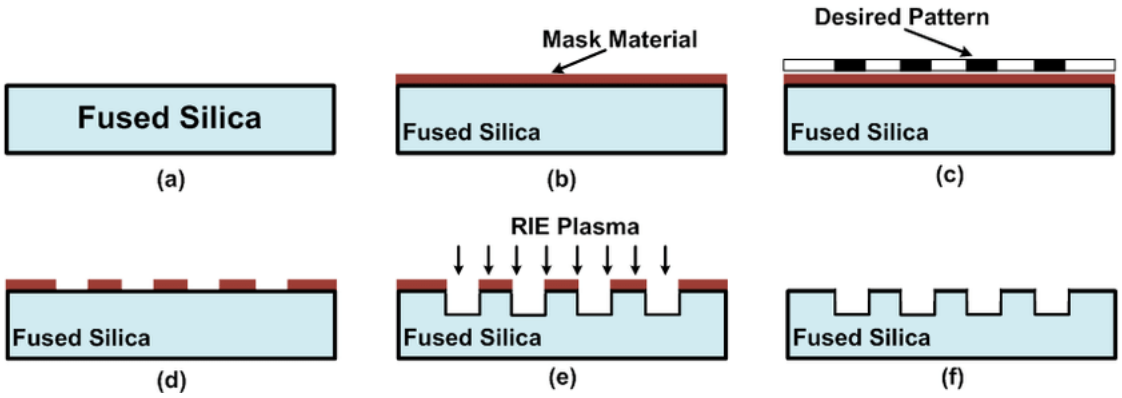

Figure 2.11: Schematic of RIE used on fused Silica. In our case instead of the silica is the Si/SiO_2 substrate and the stack on top. In steps c) to d) is being created the etch mask, in our case made of PMMA.

Meanwhile, we tried other methods for etching MBT, such as wet etching with acids, that etched the falke underneath the PMMA as well. At the end we selected Ar ion milling, which is a method that ionizes Ar atoms at low pressure and bombard the sample with the ions thanks to an electromagnetic field. The problem with this method is that, since it is physical, it etches almost everything (including the substrate itself and the etching mask) and each material has a different etch rate. The etch rate for MBT was calculated through different experiments and is of 5nm/min approximately. The fact that this method damages the substrate can lead to issues for the the global Si back gate: these areas cannot touch the contacts.

To sum up the whole process, we first etch the graphite and the hBN using RIE and then the MBT using Ar ion milling. For etching with the Hall Bar shape (following the idea of Figure

2.7), we cover the chip with PMMA and using EBL we create an etching mask, covering the parts that we want to conserve. Note that when etching we will keep the Al_2O_3 layer under the MBT: since it is non conductive, it won't interfere with the measurements.

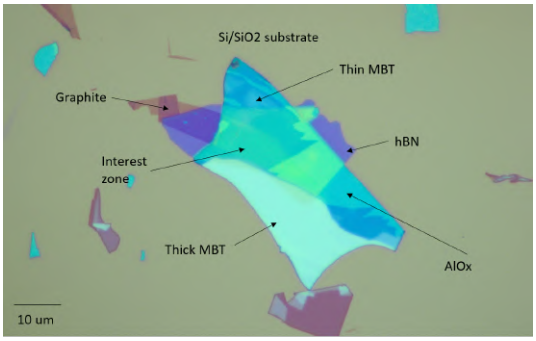

(a) Stack of MBT (with thin and thick part), hBN and graphite

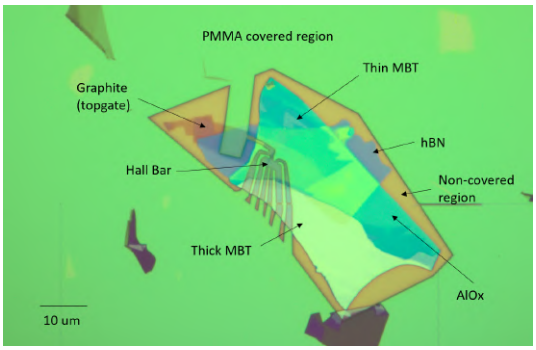

(b) Etching mask made of PMMA on top of the stack

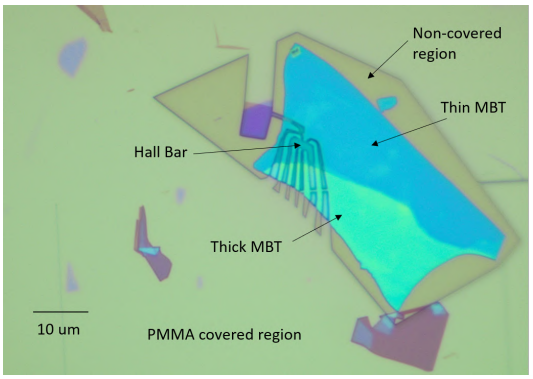

(c) After RIE, exposed hBN and graphite have been etched

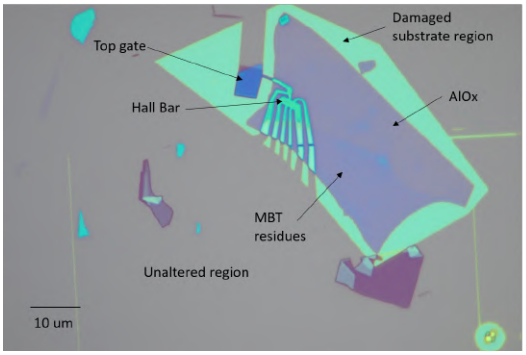

(d) After Ar ion milling, exposed MBT has been etched and the substrate damaged

Figure 2.12: Etching steps for our devices

We show the whole etching procedure in Figure 2.12:
-a) The stack on MBT, hBN and graphite (in that order from bottom to top) depicted in Figure 2.7b. The MBT has a thin and a thick part, so we place the contacts on the thick part and the thin part is protected by hBN (as the slightly different color indicates).
-b) We have created the etching mask using EBL. The Hall Bar is on the thin MBT region, the contacts are on the thick MBT part and the top gate contact is on the graphite outside the MBT. Part of the substrate is also covered to avoid the future contacts from touching the damaged areas after etching.
-c) The double recipe of RIE has effectively etched the hBN and the graphite outside of the Hall Bar and the top gate region. hBN is still protecting the region of interest.
-d) Ar ion million has etched the exposed MBT, leaving the Al_2O_3 naked. We can also see that the areas where the Si substrate was exposed are damaged, but contacts can still be

evaporated through unaltered areas. After etching, the remaining part is to evaporate the contacts.

2.6 Summary of nanofabrication

This section presents the whole process of nanofabrication in chronological order. For illustrating it, the evolution of the device presented in Figure 2.12 is used as example:
-A) We needed to exfoliate the materials. For MBT, we exfoliated the crystal inside the glovebox on kapton tape, that we placed in the e-beam Evaporator (which is inside the glovebox as well). We evaporated the 50nm of Al_2O_3 slowly and we kept following the steps described in Figure 2.1, stopping when the flakes were on the PDMS.
We also exfoliated graphite and hBN in the fabrication lab using their standard methods.
-B) We flakehunted the MBT on the PDMS and the chips of hBN and graphite. We selected the MBT that have the ideal conditions: large interest area of 2 or 4 SL and a thicker part connected to it (2SL in this example). Then following the shape and size of those areas we selected an hBN flake and a finger-shaped graphite for the top gate. All three flake is presented in Figure 2.13a.
-C) We made the design and we transfered the MBT to a Si chip by just pressing the PDMS region where the flake is, using a transfer set-up. The graphite and the hBN were then stacked using the same set-up and a PC slide, making sure to maintain the alignment we planned and finally we melted the PC on the MBT chip. The PC was removed thanks to chloroform. These steps are depicted in Figure 2.13 b, c& d.
-D) We took an Atomic Force Microscope scan of our interest regions to check the bubbles that may have formed during the transfer: we wanted to avoid them as much as possible in the design in order to make a cleaner device. The finished stack is shown in Figure 2.14a.
-E) We brought our chip to the EBL after it was covered in PMMA and we developped our design (checking wether the alignment was correct). We followed by the RIE etching for the graphite and for the hBN and then the Ar ion milling for the MBT. The result can be seen in Figure 2.14b.
-F) We evaporated the Cr/Au (5nm of Cr, 80nm of Au, since we needed it to be thicker than the flake). For that we needed to cover again the chip in PMMA and "draw" the pattern with EBL. We used the thermal evaporator to deposit the metals and the device is complete. The PMMA design and evaporated contacts are in Figure 2.14c & d.
-G) We wire-bond the device to a chip carrier and placing it in a measurement set-up.

(a) MBT flake on PDMS with 2SL layer area and a thicker area next to it

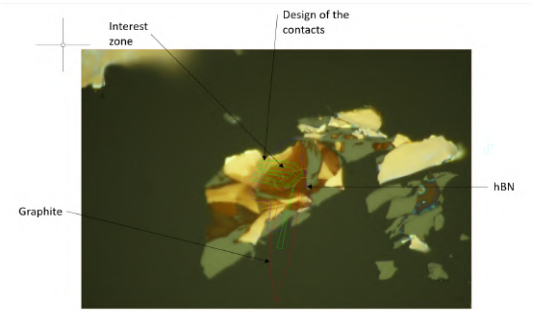

(b) Example of design on AutoCAD (another device)

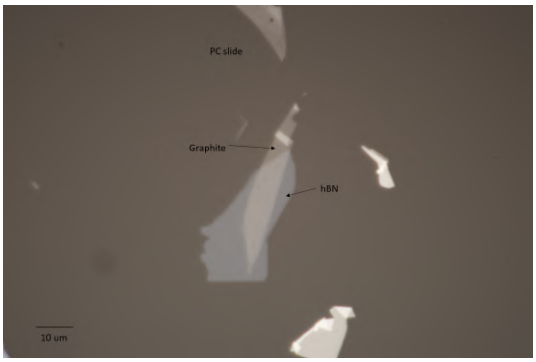

(c) Stack of hBN and graphite on the PC slide. As we can see, the graphite folded during the transfer process

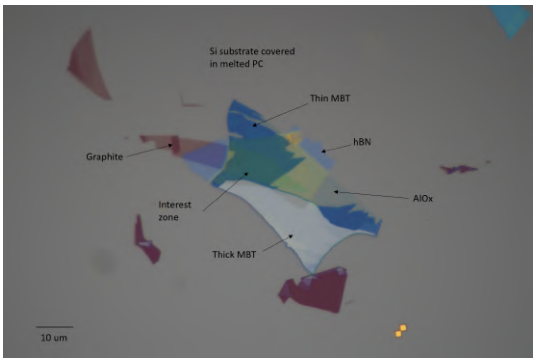

(d) Stack of MBT, hBN and graphite on the substrate with the PC melted

Figure 2.13: From flakehunting to stacking

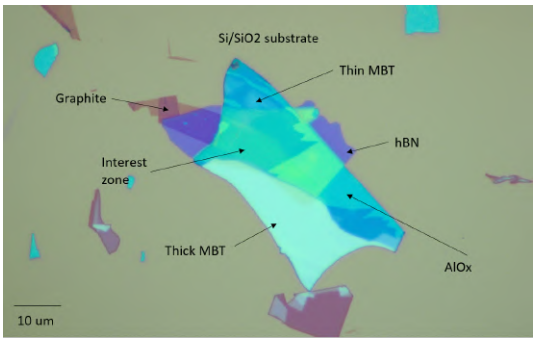

(a) Stack of MBT (with thin and thick part), hBN and graphite

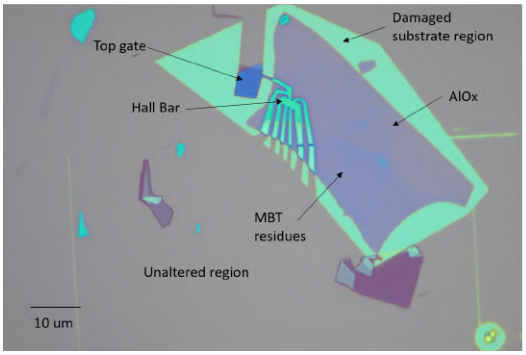

(b) Device after finishing etching

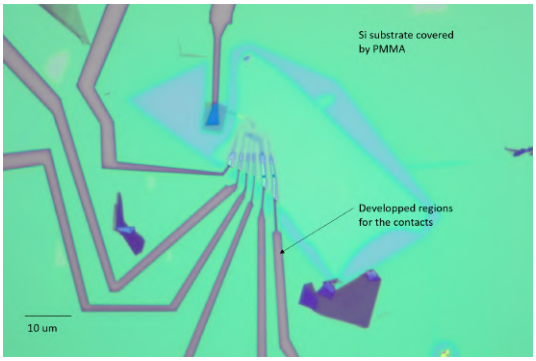

(c) Pattern for the contacts on the chip (previous to evaporation), Hall bar seen with the big objective

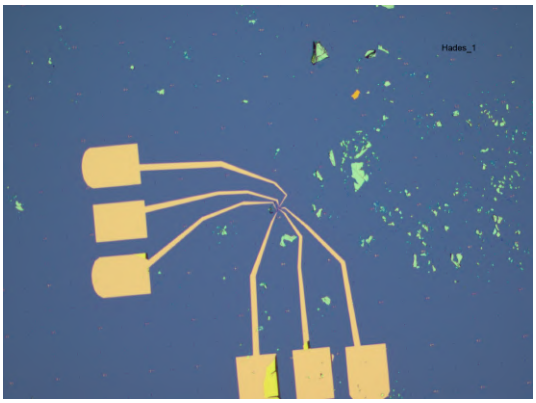

(d) With the Cr/Au evaporated (this one is another device), small objective

Figure 2.14: From etching to evaporation

Chapter 3

Results

In this chapter we present the different batches of our devices and the transport measurement results, as well as the two collaborations that are ongoing at the moment. We measured all these results in a He3 fridge reaching down to 0.3K and with a variable out of plane magnetic field.

3.1 First generation of devices

The first generation of devices is a very simple one, a first test with MBT. The flakes were obtained with the most basic exfoliation method, just covering the substrate with a thin layer of Ti and Al_2O_3 as explained in Section 2.1. We tried to minimize the exposure to air, but the device was not encapsulated and the top contacts were made of Ti/Au. The flakes were the thinnest we could find using this exfoliation method, but still too thick, around 9-10SL. Figure 3.1 shows some of the devices of this first batch.

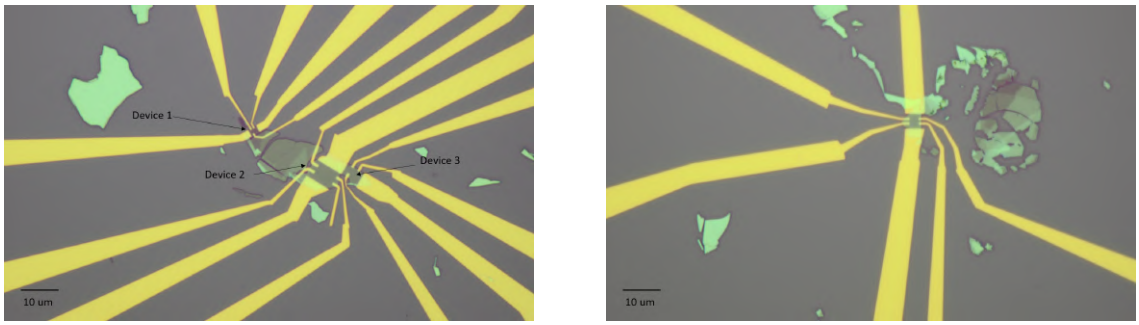

(a) 3 devices on a single flake

(b) Another device

Figure 3.1: Some of the devices from the first batch

Once these devices were in the measurement set-up, their resistance turned out to be of a few

tens of $M\Omega$ at room temperature, 3 orders of magnitude higher than expected. Oxidation due to overexposure to air or bad contacts are likely to be the main reasons that could cause this huge resistance.

The solutions we implemented for future devices are the following:
-Minimizing the exposure to air as much as possible. Note that it is impossible to avoid it at 100% without encapsulating since for inserting it in the thermal evaporator or in the EBL, it still needs to be exposed for a short period of time.
-Changing to Cr/Au contacts.

3.2 Second Generation of devices

For this generation the changes above mentioned were implemented and other tests were made: we fabricated thicker devices to check if the oxidation was still a problem, since thicker devices are supposed to maintain conductivity even if slightly oxidized. If the thinner devices had huge resistance and not the thick ones, it is likely that oxidation was still an issue even with the minimization of the exposure to air. We also fabricated an encapsulated device, using bottom contacts, a back gate and a top gate. In Figure 3.2 we can see a thinner device with top contacts and the encapsulated device.

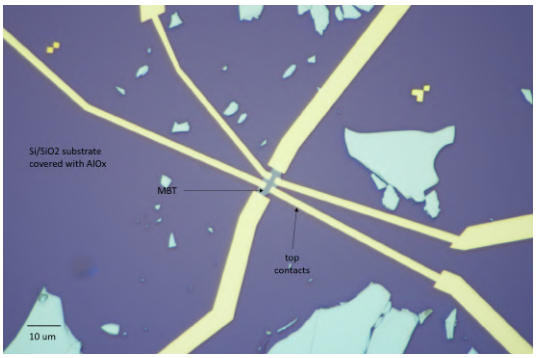

(a) Device 2a: top contacts and 11SL thick MBT

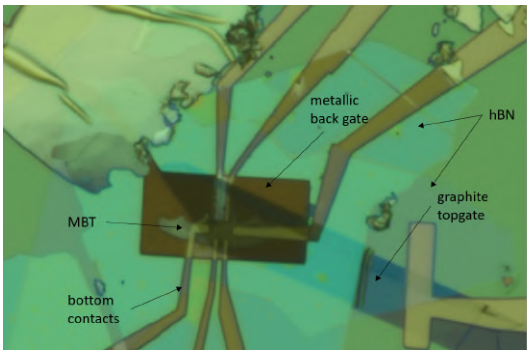

(b) Device 2b: Encapsulated device with bottom contacts and 8SL thick (the imaged is zoomed). There is a rectangular metallic back gate and a graphite top gate

Figure 3.2: Second generation devices

For this generation the resistance results were in the order of the $k\Omega$ as expected, but unfortunately, for the device 2b in Figure 3.2, the two contacts for measurement on the top are not touching the flake due to a misalignment, so we could not measure the Hall resistance for that device.

We first analyze the results for the device 2a, for which the Si substrate is used as a global back gate (Figures 3.3 and 3.4):
In Figure 3.3a, there are two horizontal lines, in both R_{xx} (longitudinal resistance) and R_{yx} (Hall resistance) around 2.5 and -2.5 T. These lines are the transition from AFM to FM and vice versa so between -2.5 and 2.5 T (approx) the MBT is in AFM configuration and outside of that range the device is in FM configuration, forced by the high magnetic field. Those two transitions are also observed in the cuts in Figure 3.3b. We also can identify a magnetic hysteresis loop in R_{yx} and QAH effect when the magnetic field is sweeped in both directions, proof that there is a magnetization in the sample, as expected since the device 2a has 11SL.

A closer look at the transition FM/AFM seemed interesting to check if that transition was flat (i.e. independent of the global back gate voltage V_B) or if it depended on the electric field (so probably on V_B). To do so, in Figure 3.4 the B and V_B dependence of R_{xx} was remeasured, but zooming on the transition region (Figure 3.4a) and then the derivative with respect to B was calculated in order to enhance the transition for each V_B (Figure 3.4b). As can be seen in Figure 3.4b, there is a huge area of change (in yellow), which is the FM/AFM transition and it seems to be a little curved, meaning that it depends on V_B. This first result suggests that the electric field has an influence in the FM/AFM transition, so, if we tune the magnetic field, we can cross the transition just by E field.

The device 2b has both top and back gates so we can independently tune the electric field and the carrier density since there is a linear conversion from one pair to the other. We cannot measure the Hall resistance due to a stacking mistake.
In Figure 3.5 R_{xx} is measured at B = 0 T sweeping the bottom (V_B) and the top (V_T) gates voltages. The Dirac point is the point of higher resistance and it is placed at the origin for the electric field E and the carrier density n coordinates, so the reference system can be changed to those two variables.
In Figure 3.6, the FM/AFM transition is studied depending on E and n. The FM/AFM transition is represented in a) and b) by the high contrast vertical lines around -3 and 3 T (so AFM between those two, FM outside that box). Unfortunately, the transition does not seem to change with E as it can be seen from Figure 3.6c. The reasons for that are still unclear and it is unfortunate not having access to R_{yx} for more information. We can nevertheless see another interesting feature in c): since the sweeps in both directions have been overlapped, the presence of little steps close to 0 T is highlighted. Those seem to be rearrangements in the different layers just as seen in the Figure 1.7 from [9].

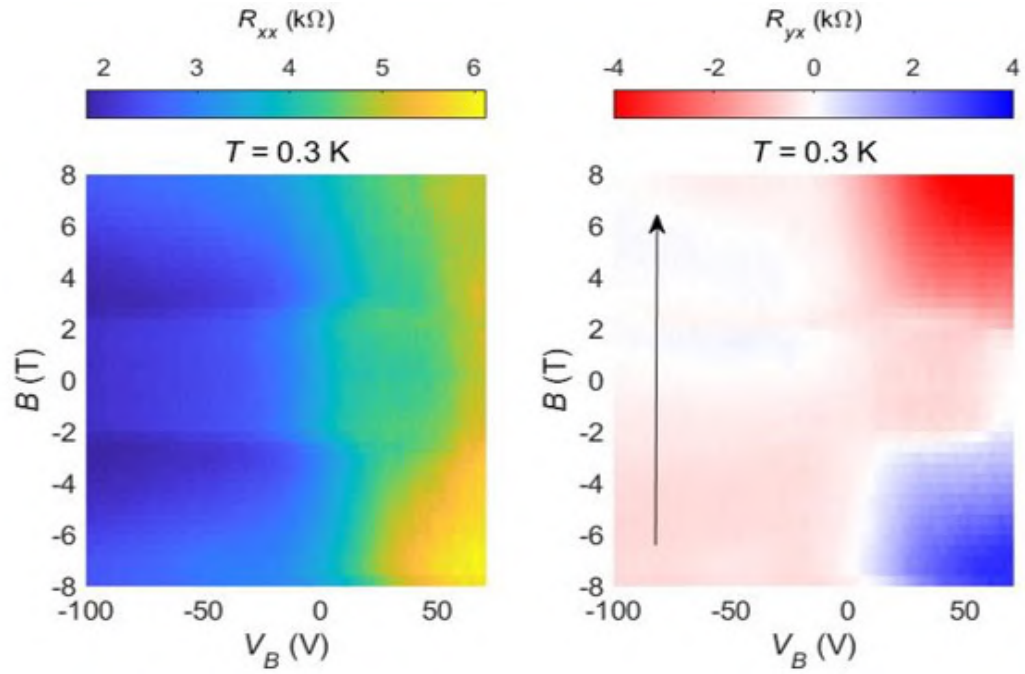

(a) Longitudinal and Hall Resistance respect to the magnetic field B and the global back gate voltage V_B

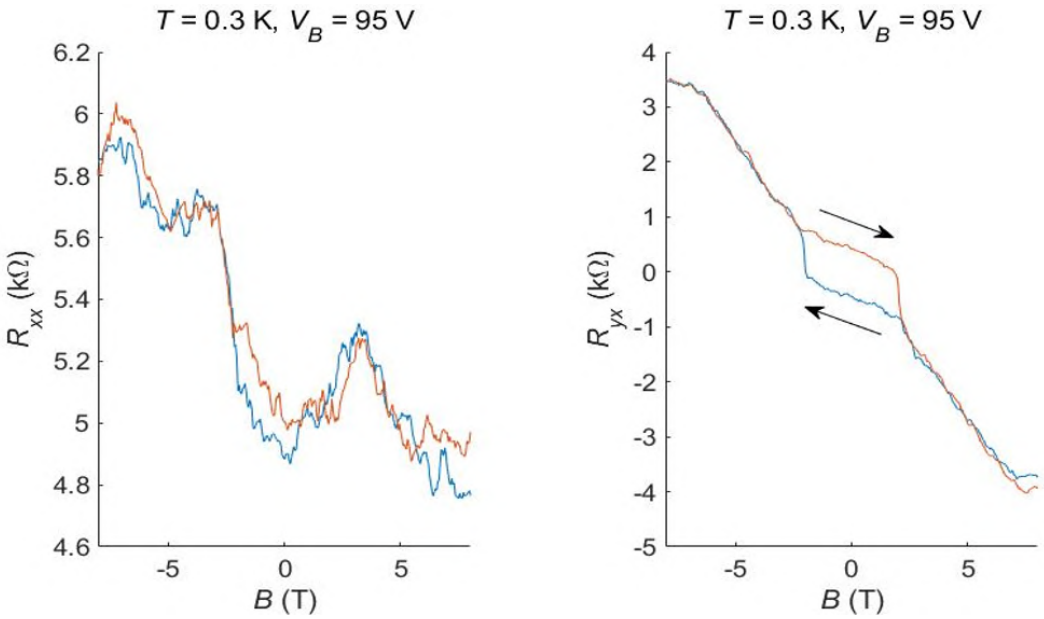

(b) Cuts of the previous color map at $V_B = 95V$, sweeeping B in both directions

Figure 3.3: Measurements for device 2a (11SL) at $T = 0.3$ K, both longitudinal (left) and Hall (right) resistance. In a) is a scan from -100 to 95 V for the global back gate V_B and from -8 to 8 T. In b) a cut of the previous scan for $V_B = 95$ V and sweeping the magnetic field from -8 to 8 T and back to -8 T (orange and blue resp.). The Hall resistance has been antisymmetrized.

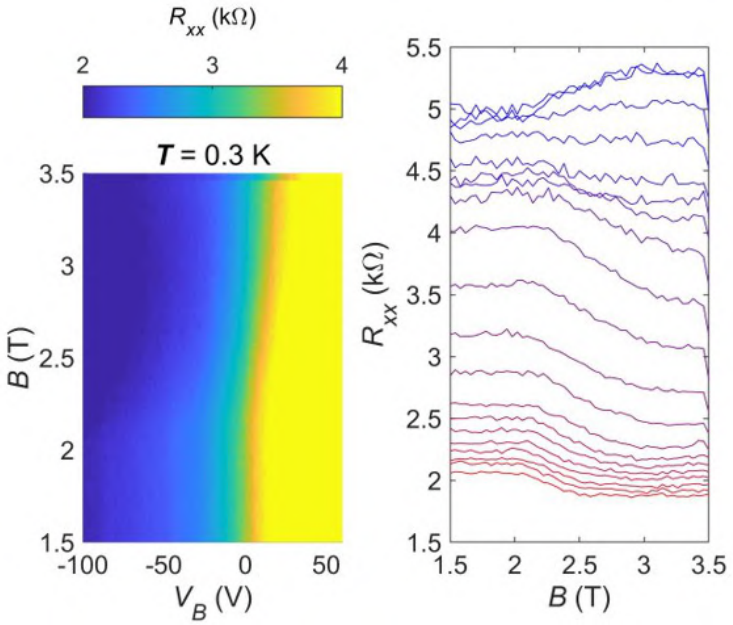

(a) Zoom on the transition region

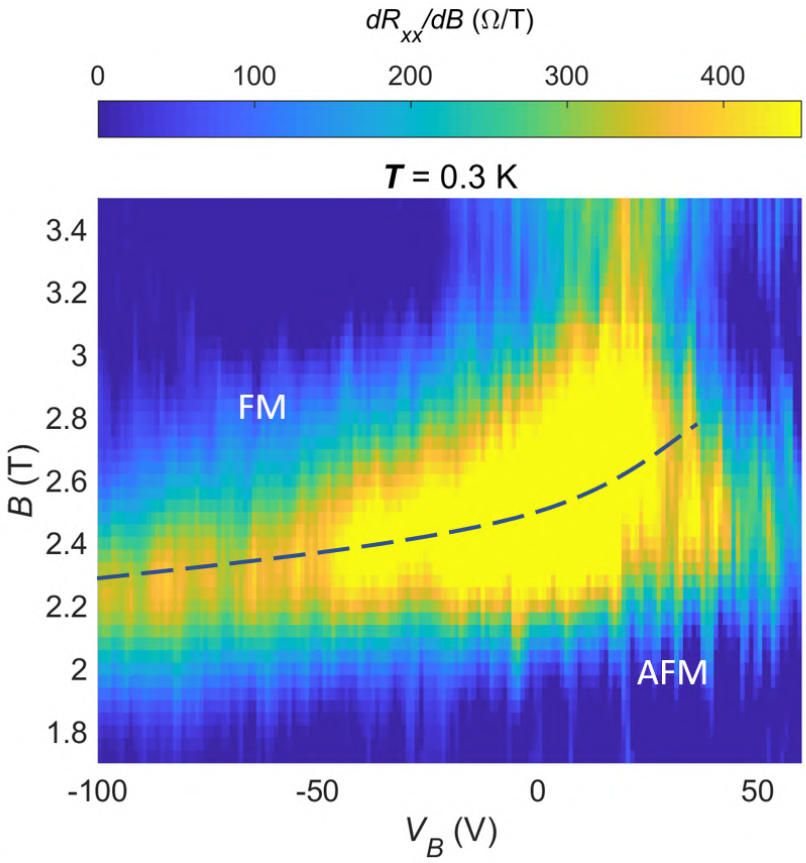

(b) Derivative of the longitudinal resistance

Figure 3.4: Measurements for device 2a (11SL) at $T = 0.3$ K. In a) is a zoom of the previous Figure 3.3 longitudinal resistance in the region of the FM/AFM transition (in color map and its cuts). In b) is the derivative of the top picture respect to the magnetic field (so on the vertical direction); this derivative has been smoothed for diminishing noise.

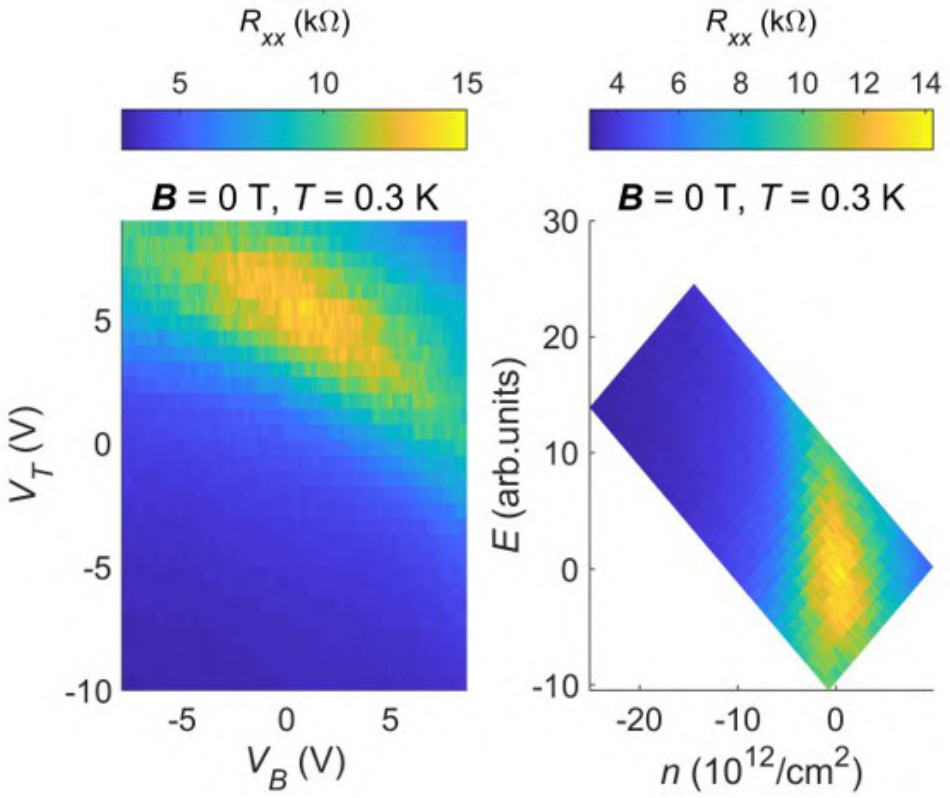

Figure 3.5: Measurements for device 2b (8SL) at $T = 0.3$ K and B = 0 T. On the left the measurement of R_{xx} sweeping the top and back gates. On the right the same sweep, but changing to E (electric field) and n (carrier density) coordinates.

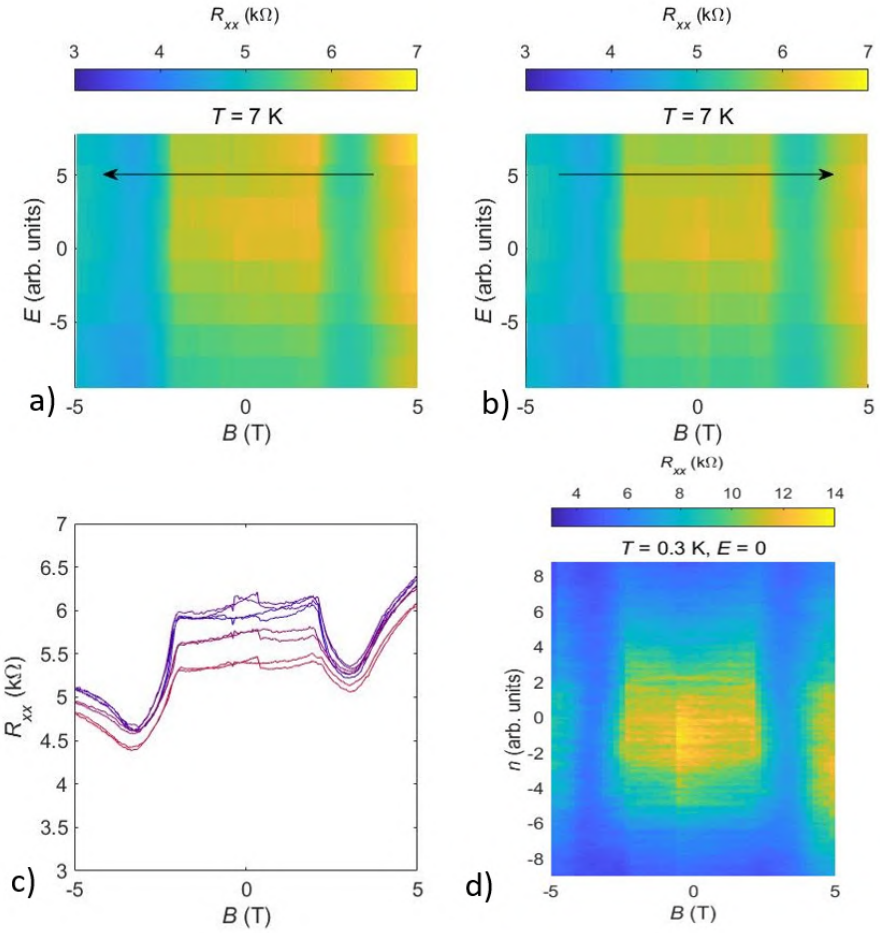

Figure 3.6: Measurements for device 2b (8SL). a) and b) represent the measurement of R_{xx} sweeping the electric field and the magnetic field (changing the direction of sweeping of the magnetic field). c) is the cuts of a) and b). d) is the measurement of R_{xx} sweeping the carrier density n and the magnetic field.

3.3 Third generation of devices

This is the first generation using the Al_2O_3 assisted exfoliation technique and therefore the thickness of the obtained MBT flakes is much lower, so 2 to 4SL thick devices were targeted. The devices were not yet etched, but some of them have been tip-cleaned to give them a better shape. A contact was left open for, in a future, being able to encapsulate and put a top gate. Those devices use the Si substrate as a global back gate. They are in general very simple, mostly for testing the new exfoliation technique.
Figure 3.7 presents the 4 devices made in this generation, although only the two marked by an arrow were actually measured.

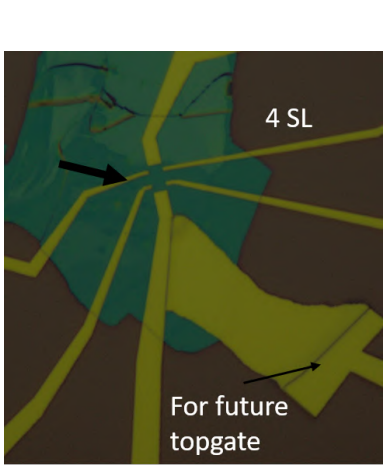

(a) Device 3a. A problem during lift off did not completely separated the "future top gate" contact to a Hall Bar contact.

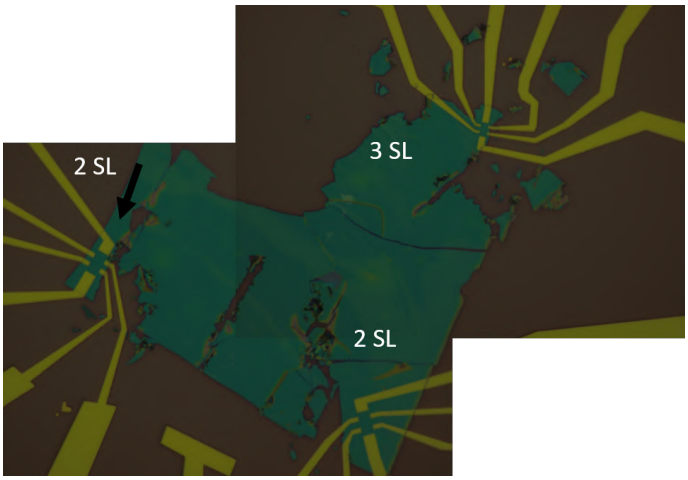

(b) 3 devices on a single flake, from left to right 3b, 3c, 3d. They have been tip cleaned (as the residues indicate) to give them a better Hall bar shape. The original flake is the one in Figure 2.3 bottom.

Figure 3.7: The third generation devices. The arrows indicate the ones that have been measured.

Looking at the measurements for the device 3a in Figure 3.8, they are very noisy. This noisy aspect might be coming from the large contact resistance. In the R_{xx} color map the Dirac point is clear, where the resistance is maximal. A hysteresis loop can also be seen, evidence that there is some magnetization. Due to the fact that the number of SL is even, we should not expect to measure this loop, but since the measurement of the thickness was also uncertain at that time, it could be possible to have a 3 or 5SL sample, or it could be a non-trivial rearrangement of the internal magnetization of the layers.

For the device 3b, the results are unclear. As presented in Figure 3.9 the sample quickly becomes insulating, maybe due to oxidation and the results are mostly invalidated by that high resistance.

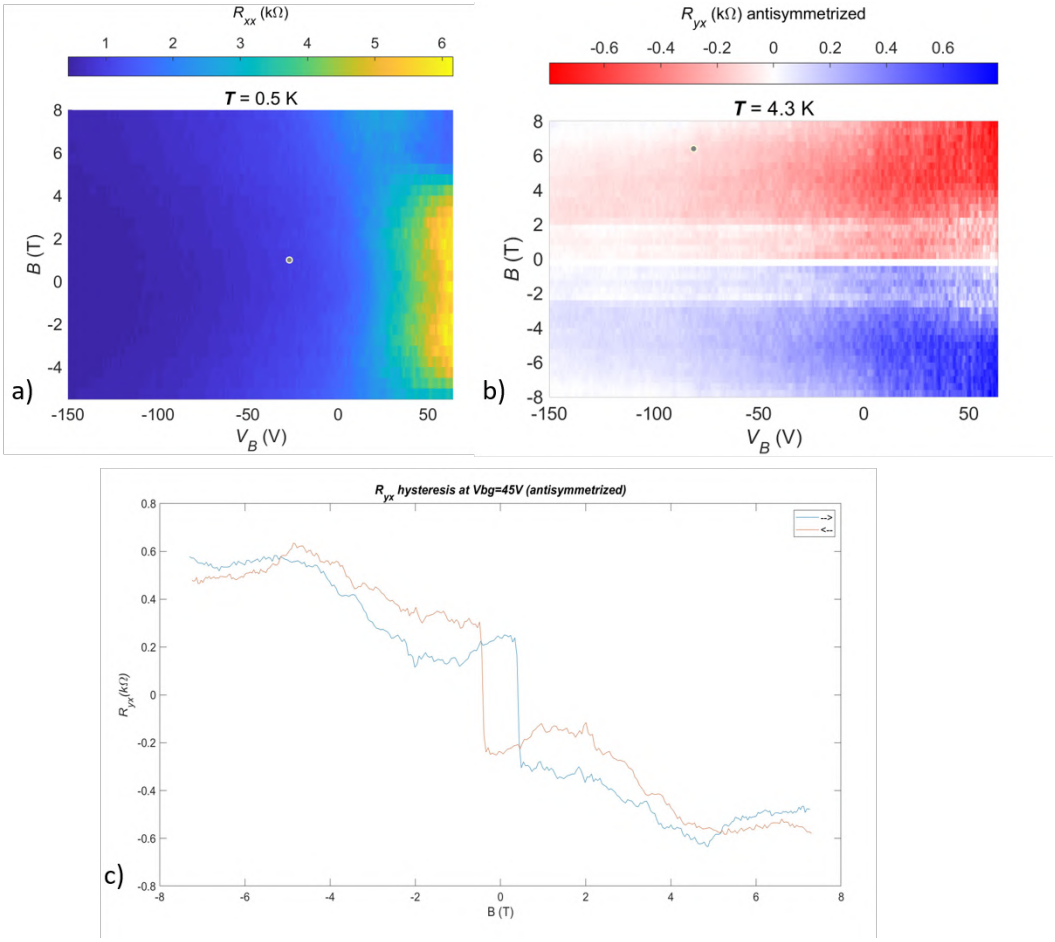

Figure 3.8: Measurements for device 3a (4SL). a) and b) represent the measurement of R_{xx} and R_{yx} resp. sweeping the global back gate voltage and the magnetic field . c) represents R_{yx} sweeping the magnetic field in both directions (antisymmetrized) at $V_B = 45$V.

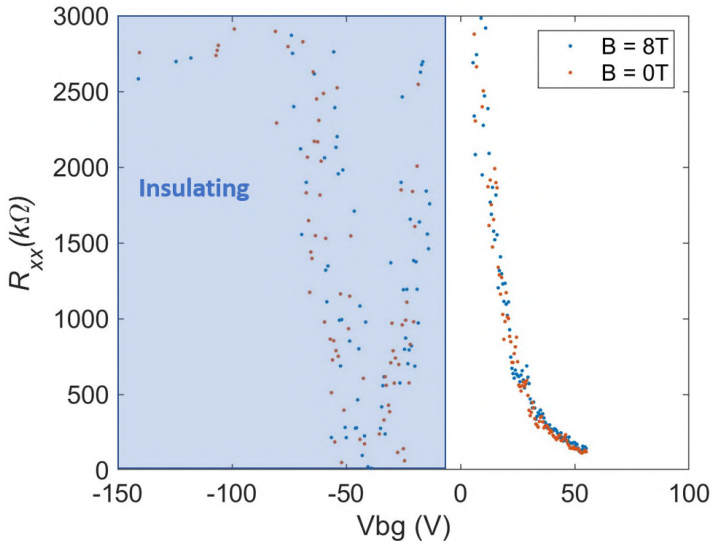

Figure 3.9: Measurements for device 3b (2SL). The device turns insulating very fast.

3.4 Fourth generation of devices

This fourth generation is the last one we fabricated and is the one where all the developed methods were applied: Al_2O_3 assisted exfoliation method, encapsulation with hBN and a graphite top gate and etching as described in Section 2.5.
Unfortunately, due to the Covid-19 pandemic situation and closing of the MIT, we could not finish the evaporation of the contacts and thus could not measure our devices. Hopefully this will be done as soon as the Universities in the Boston area reopen and we will be able to get the results for this batch.
In Figure 3.10 the devices are presented in their latest stage.

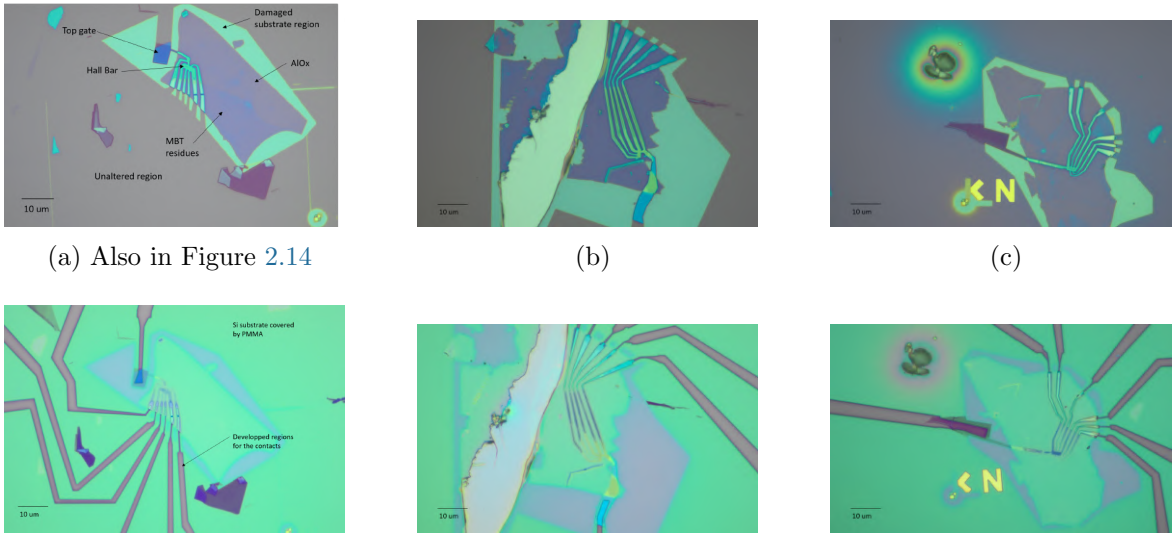

(a) Also in Figure 2.14 (b) (c)

(d) Also in Figure 2.14 (e) (f)

Figure 3.10: The fourth generation devices, on top after etching and on the bottom ready for evaporation of the contacts

3.5 Collaborations

3.5.1 Ju's group: Second Harmonic Generation

We collaborated with Tianyi Han and Tonghang Han from Long Ju's group at MIT. In this collaboration we used the Second Harmonic Generation (SHG) method, a nonlinear optical process that converts two photons of the same frequency into one photon of twice the fundamental frequency. There is two origins for a signal in SHG. The first reason (and more frequent one in measurements) is that the material's lattice is not centrosymmetric (c-SHG). The second one, used in CrI_3, is the breaking of the inversion symmetry (i-SHG). As depicted in Figure 3.11a, in the case of a AFM material, the even layered samples break the inversion symmetry whereas the odd layered do not. Above the Neel temperature, there is no magnetic ordering so the inversion symmetry still stands and there should be no signal, as we can see in Figure 3.11b for CrI_3 [19]. Since the MBT lattice is centrosymmetic, this method allows us to see the parity of the thickness of the sample.

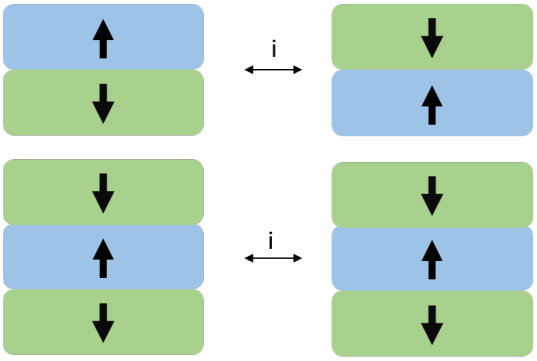

(a) Inversion symmetry for even and odd layers of an AFM material

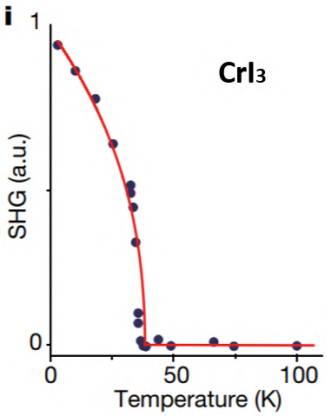

(b) SHG signal in a.u. depending on the temperature for bilayer CrI_3 (Neel temperature of 45K) Source: [19]

Figure 3.11: Inversion symmetry and SHG measurements depending on the temperature

We prepared the sample using the Al_2O_3 assisted exfoliation method and then covered the MBT by another layer of Al_2O_3 for capping it. Since Al_2O_3 is transparent, it does not cause any interference with the SGH measurements. In Figure 3.12 is presented a schematic of the encapsulation method as well as one of the flakes we provided. The flakes need to have large and flat areas of different thicknesses.

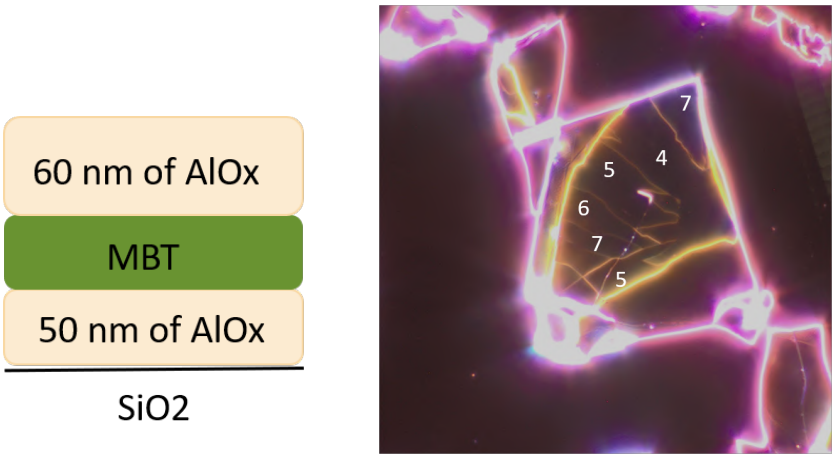

(a) Schematic of the encapsulation method

(b) The provided flake seen in Dark Field image with the number of SL written in white

Figure 3.12: A sample provided for the SHG measurements and its schematic

The results were not as expected. A signal appeared also at room temperature as it can be seen in Figure 3.13a. This signal is also present at $T = 4$ K, overlapping with the targeted signal and thus obtaining a non-zero value for all the sample, even and odd parts. Judging from the pattern of the signal (6 folded, which related to the internal structure of the crystal), it appears to be coming from the crystal itself, but the exact reason is not clear yet. It might be a high number of impurities that break the inversion symmetry and therefore interfere in the measurement or it might be coming from the interface effect [20]. In Figure 3.13 some results at low temperature are shown. As the causes of this signal could not been determined nor the ways of subtracting it, we decided after a few samples to stop until that source of signal at RT is identified.

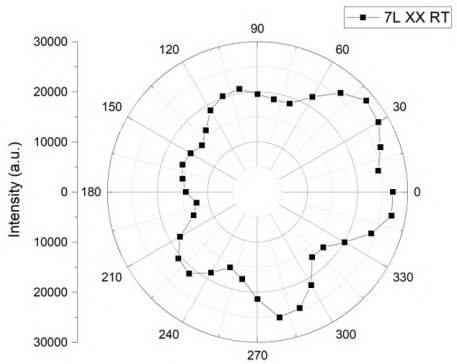

(a) XX signal at room temperature on the 7SL part of the flake in Figure 3.12

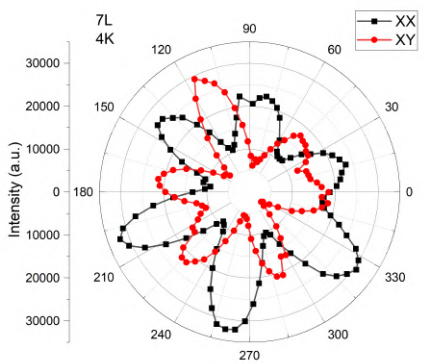

(b) XX and XY signal at $T = 4$ K on the 7SL part of the flake in Figure 3.12

Figure 3.13: The SHG signals of different areas of the sample shown in Figure 3.12.

3.5.2 Yacoby's group: N-V measurements

The Nitrogen Vacancy (N-V) center microscopy is a method that uses diamond crystals with N-V defects to explore and measure the magnetic properties of materials by moving the N-V tip on top of it [21]. We collaborated with Uri Vool and Asaf Hamo from Amir Yacoby's group at Harvard, that performed the N-V measurements on our sample of MBT.

Fabrication-wise, we needed a flake that had a few steps in a small region (5um x 5um square), changing the parity of the thickness to check that the zero net magnetization(even)/net magnetization(odd) regions could be spotted. As we need a non conductive substrate for N-V measurements, we used a quartz substrate that has a long line of gold that is used for RF delivery. We also encapsulated our flake with a thin hBN for avoiding oxidation. hBN does not interfere with the measurement.

In Figure 3.14, the flake and the different possible regions that could be measured are shown, with all the thicknesses of the flake. The hBN folded during the transfer, but interesting regions are still covered.

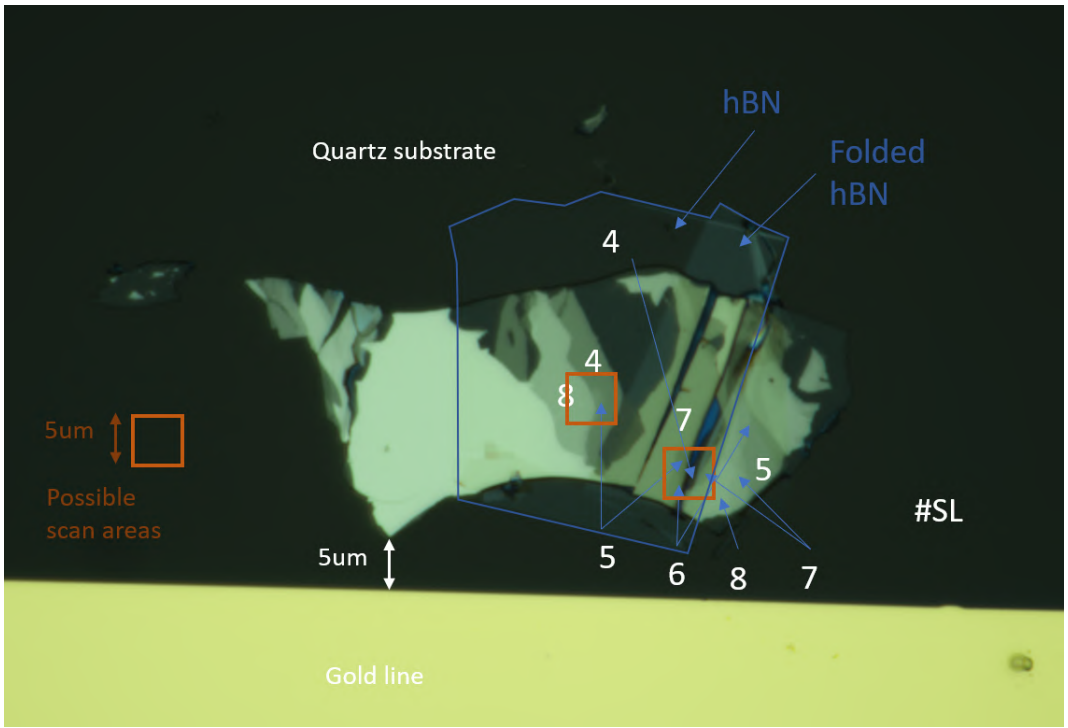

Figure 3.14: Sample for the N-V measurement. The numbers in white are the thickness in number of SL, the blue shade is the hBN that is covering the flake and the brown squares are the interesting areas for measurement.

To give an insight of how to read N-V measurements, a example of measurement on CrI_3 is shown in Figure 3.15. This method measures the magnetic field intensity aligned with the

tip, as it can be seen in Figure 3.15c, so we mostly see the edges of the magnetization layer, since as depicted in Figure 3.15a, the edges are where the magnetic field is more prominent. This magnetic field map can then be translated to a magnetization map, as in Figure 3.15d.

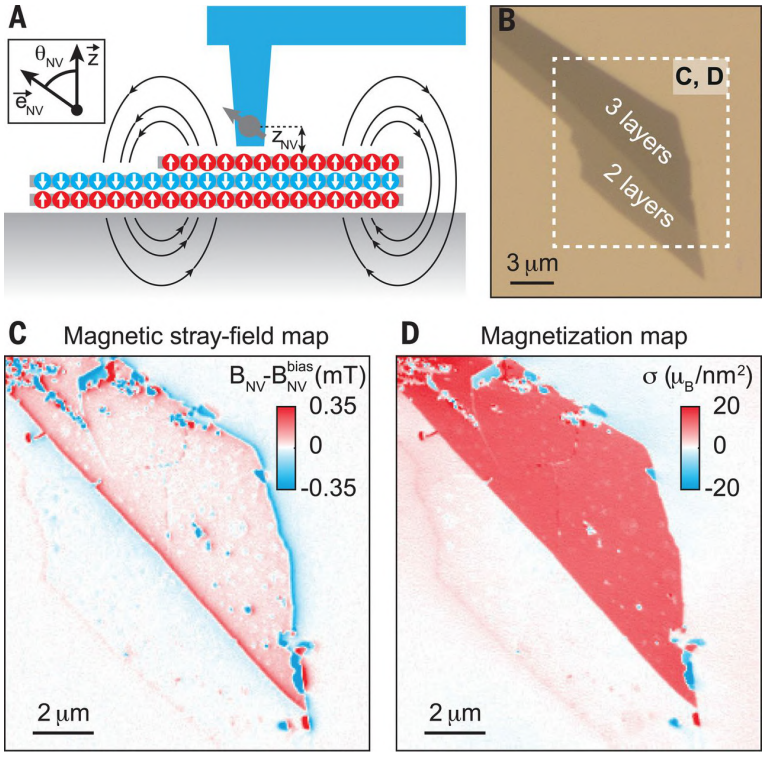

Figure 3.15: N-V measurements on CrI_3. A)Schematic of the N-V tip scanning the sample and its B field lines. B)The CrI_3 flake. C) Magnetic field map obtained after scan. D)Translation of C) to magnetization map. Source:[22]

Some preliminary and very promising measurements have been realized, but due to the world-wide pandemic, those experiments are currently on hold. Figure 3.16 depicts part of those results. Comparing these results to those shwon in Figure 3.15, it is clear that there is a magnetization in the 5SL area and no magnetization in the 4 and 8SL area. Others scans have seen that there is no magnetic field between even layers. This is exactly what was desired as preliminary results.
The other interest area of Figure 3.14 has been checked and the results are reproduced for the 5, 6 and 7SL, but we do not have the data. The next plan is to apply a high magnetic field in both directions and confirm if there is a switching of the sign of the magnetization of the MBT.

This measurement is just the start of a long collaboration. Samples with contacts and top/back gates will also be fabricated in order to see the edge current, the electrical switching of the magnetic state, etc... This method seems very promising.

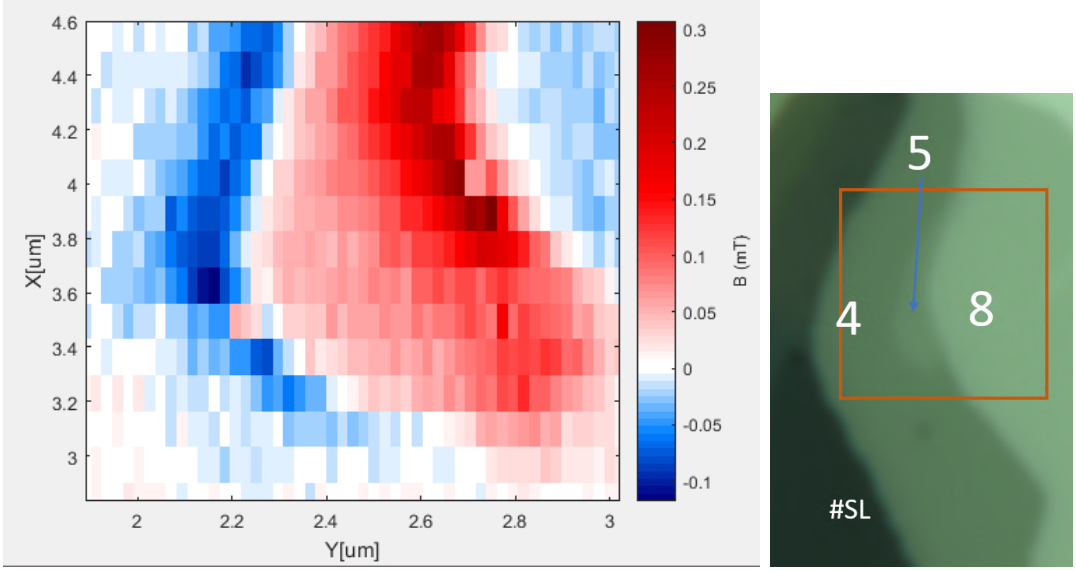

Figure 3.16: N-V measurements. The area that is being measured is the left interest area in Figure 3.14, flipped 180º and represented on the left. These measurements are done at 5K

3.6 Next Steps

The next steps are to measure the fourth and even a fifth generation of devices in order to measure all the objectives we set in Chapter 1. The collaboration with Yacoby's group is also going to continue with more sophisticated devices, in order to measure the edge current and the electrical switching of the magnetization, among other features. Once the source of the signal at room temperature in SHG will be determined, the collaboration with Ju's group will also bring us very interesting results.

Chapter 4

Conclusion

We developed a large range of fabrication techniques for MBT devices, a new and very interesting material that is being widely studied at this moment. Several MBT devices were made, following the techniques described in Chapter 2. At first very simple devices, tests on MBT, since our team started from scratch on this material at my arrival. Then the fabrication became more elaborated, with the introduction of the Al_2O_3 assisted exfoliation method and later on the development of etching techniques for the MBT/hBN/graphite. Two new collaborations are ongoing. The first one for measuring the SHG of MBT and the second one for studying the magnetization of MBT thanks to N-V measurements, with encouraging results.

The measurements realized on our samples gave us a first glance at the AHE, at the magnetization of MBT and at the AFM/FM transition. This results are part of the objectives presented in Chapter 1. As the devices are getting better and better, we hope to measure all the other objectives we set, but this a long and difficult task that will continue after the end of my stay at MIT. The Covid-19 pandemic and closing of MIT unfortunately stopped our progression in its more productive moment, but the ground is ready for a rapid resumption of the study.

Bibliography

[1] Vladimir Litvinov, Magnetism in Topological Insulators, *SPringer Editions* (2020)

[2] B. Andrei Bernevig and Taylor L. Hughes, Topological Insulators and Topological Superconductors, *Princeton University Press* (2013)

[3] Moore, Joel E., The birth of topological insulators, *Nature* **464**, 94–198 (2010)

[4] Y. Tokura, K. Yasuda, A. Tsukazaki, Magnetic topological insulators, *Nat. Rev. Phys.* **1**, 126-143 (2019)

[5] C.Z. Change et al., Experimental Observation of the Quantum Anomalous Hall Effect in a Magnetic Topological Insulator, *Science* **340**, 167-170 (2013)

[6] D. S. Lee et al., Crystal structure, properties and nanostructuring of a new layered chalcogenide semiconductor, Bi2MnTe4, *Cryst. Eng. Commun.* **15**, 5532- 5538 (2013)

[7] Yan, J. Q. Yan et al., Crystal growth and magnetic structure of MnBi2Te4, *Phys.Rev. Mater.* **3**, 064202 (2019)

[8] Hao Li et al., Antiferromagnetic Topological Insulator MnBi2Te4: Synthesis and Magnetic properties, *arXiv:1907.13018* (2019)

[9] Deng et al.,Quantum anomalous Hall effect in intrinsic magnetic topological insulator MnBi2Te4, *Science* **367**, 895-900 (2020)

[10] Nicodemos Varnava et al., Surfaces of axion insulators, *Phys. Rev. B* **98**, 245117 (2018)

[11] S. Jiang et al., Electric-field switching of two-dimensional van der Waals magnets, *Nature Materials* **17**, 406-410 (2018)

[12] Bevin Huang et al., Electrical Control of 2D Magnetism in Bilayer CrI3, *Nature Nanotechnology* **13**, 544-548 (2018)

[13] Chang Liu et al., Robust axion insulator and Chern insulator phases in a two-dimensional antiferromagnetic topological insulator, *Nature Materials* **19**, 522–527 (2020)

[14] Shiqiao Du et al., Berry Curvature Engineering by Gating Two-Dimensional Antiferromagnets, *arXiv:1909.01194* (2019)

[15] Deng et al., Anisotropic magnetocaloric effect in $Fe_{3x}GeTe_2$, *Scientific Reports* **9**, 13233 (2018)

[16] O. Karazova et al., Epitaxial Graphene and Graphene–Based Devices Studied by Electrical Scanning Probe Microscopy, *Crystals* **3**, 191-233 (2013)

[17] Cao, Y. et al. Unconventional superconductivity in magic-angle graphene superlattices, *Nature* **556**, 43–50 (2018)

[18] E. J. Telford, Via Method for Lithography Free Contact and Preservation of 2D Materials, *Nano Letters* **18**, 1416-1420 (2018)

[19] Z. Sun et al., Giant nonreciprocal second-harmonic generation from antiferromagnetic bilayer CrI_3, *Nature* **572**, 497–501 (2019)

[20] Dimitrios Damianos, Second harmonic generation (SHG) for contactless characterization of dielectricsemiconductor interfaces, *Micro and nanotechnologies/Microelectronics*, Université Grenoble Alpes, (2018)

[21] Cheong, S. et al., Seeing is believing: visualization of antiferromagnetic domains, *npj Quantum Mater.* **5**, 3 (2020).

[22] L. Thiel et al., Probing magnetism in 2D materials at the nanoscale with single-spin microscopy, *Science* **364**, 973-976 (2019)

Appendices

Appendix A

Electric field Model

The model aims to estimate the electric field in a MBT sample, encapsulated between two flakes of hBN, with a top and a back gate. Figure A.1 schematizes our stack and introduces the notation.

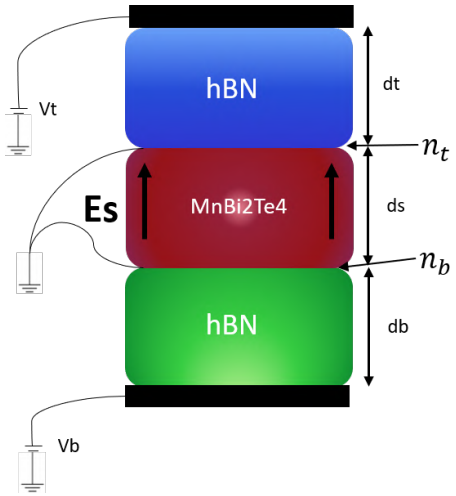

Figure A.1: Stack for the electric field model. V_t and V_b are the top and bottom gate voltages resp., dt, ds, db are the thicknesses of each layer. n_t, n_b are the carrier densities on the top and bottom resp.

Using Gauss' law at both interfaces between MBT and hBN we get, with e the absolute charge of the electron:

$$en_T = E_t - E_s \qquad en_b = E_s - E_b$$

Assuming than MBT and the hBN behave as insulators:

$$E_T = \frac{E_{F_t}/e - V_t}{dt} \qquad E_b = \frac{V_b - E_{F_b}/e}{db} \qquad E_s = \frac{E_{F_b} - E_{F_t}}{eds}$$

with E_{F_t}, E_{F_b} Fermi levels of the top and bottom resp.

Manipulating we obtain:

$$n_T = \frac{E_{F_t}}{e^2}(\frac{1}{ds} + \frac{1}{dt}) - \frac{E_{F_b}}{e^2 ds} - \frac{V_t}{edt} \qquad n_b = \frac{E_{F_b}}{e^2}(\frac{1}{ds} + \frac{1}{db}) - \frac{E_{F_t}}{e^2 ds} - \frac{V_b}{edb}$$

Now, assuming that the conduction and valence band form a cone just like in Figure 1.3, that the Fermi velocity v_F is constant and using the fact that $n = \int_0^{E_F} n(E)dE$ (we put 0 at the center of the cone), we get:

$$n_i^2 = \frac{E_{F_i}^2}{4\hbar^2 v_F^2 \pi \epsilon}$$

Using the fact that $n_i < 0 \Leftrightarrow E_{F_i} > 0$ we finally have:

$$E_{F_t} = -sign(n_t) 2\hbar v_F \sqrt{\pi} \sqrt{|\frac{\epsilon}{e^2}(E_{F_t}(\frac{1}{ds} + \frac{1}{dt}) - \frac{E_{F_b}}{ds} - \frac{eV_t}{dt})|}$$

$$E_{F_b} = -sign(n_b) 2\hbar v_F \sqrt{\pi} \sqrt{|\frac{\epsilon}{e^2}(E_{F_b}(\frac{1}{ds} + \frac{1}{db}) - \frac{E_{F_t}}{ds} - \frac{eV_b}{db})|}$$

And finally we reuse:

$$E_s = \frac{E_{F_b} - E_{F_t}}{eds}$$

We run these equations and get the results presented in Figure A.2. As expected, the intensity of the E field decreases with the thickness of the MBT very fast, so we decided that for measuring all the magnetoelectric effects, the thinner the MBT the better, for having a large range of values for E. Once the nanofabrication methods will be dominated, we will try to build devices from 2 to 4SL.

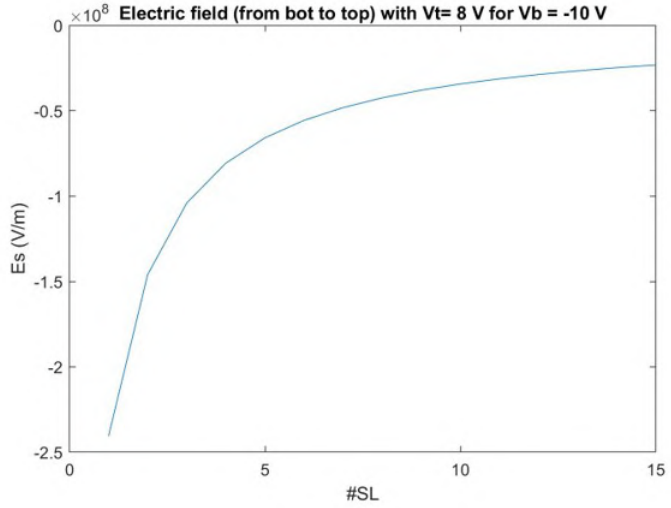

(a) Electric field inside the MBT depending on the number of SL

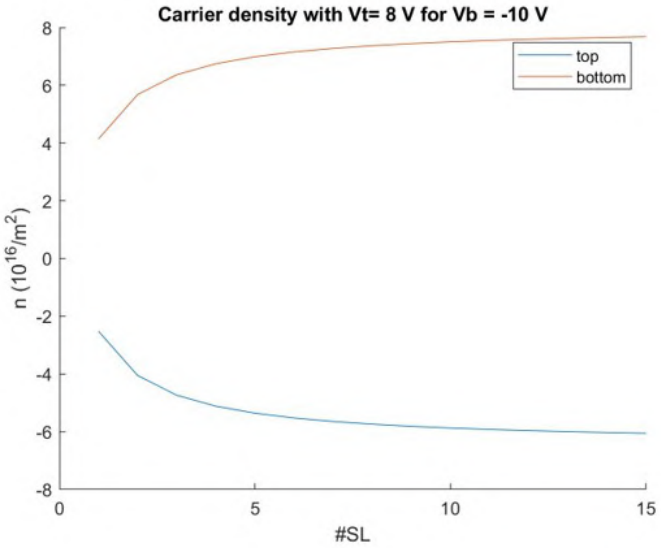

(b) Carrier density on top and bottom interface depending on the number of SL

Figure A.2: Results for the electric field model assuming a thickness of $dT = db = 20nm$ and $V_T = 8V$ and $V_b = -10V$